Can We Reconstruct Mean and Eddy Fluxes from Argo Floats?

Christopher C. Chapman, Jean-Baptiste Sallée

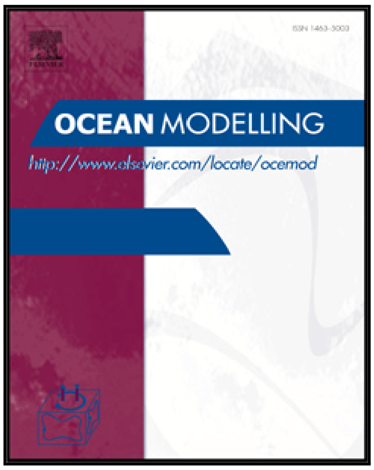

Can We Reconstruct Mean and Eddy Fluxes from Argo Floats?

Christopher Chapman, Jean-Baptiste Sallée

PII: S1463-5003(17)30148-8
DOI: 10.1016/j.ocemod.2017.10.004
Reference: OCEMOD 1251

To appear in: *Ocean Modelling*

Received date: 18 May 2017
Revised date: 13 October 2017
Accepted date: 15 October 2017

Please cite this article as: Christopher Chapman, Jean-Baptiste Sallée, Can We Reconstruct Mean and Eddy Fluxes from Argo Floats?, *Ocean Modelling* (2017), doi: 10.1016/j.ocemod.2017.10.004

Highlights

- Virtual floats show that it is possible to reconstruct interior flow using Argo floats
- The reconstruction is sensitive to temporal sampling, number of floats and time span
- The cross-Polar Front heat flux is determined using Argo floats to be 2 p/m 0.5 TW
- Heat-flux is concentrated near large bathymetry

Can We Reconstruct Mean and Eddy Fluxes from Argo Floats?

Christopher Chapman[a,*], Jean-Baptiste Sallée[a]

[a]*LOCEAN-IPSL*
Université de Pierre et Marie Curie, Paris CEDEX 75252,France.

Abstract

The capacity of deep velocity estimates provided by the Argo float array to reconstruct both mean and eddying quantities, such as the heat flux, is addressed using an idealized eddy resolving numerical model, designed to be representative of the Southern Ocean. The model is seeded with 450 "virtual" Argo floats, which are then advected by the model fields for 10 years. The role of temporal sampling, array density and length of the float experiment are then systematically investigated by comparing the reconstructed velocity, eddy kinetic energy and heat-flux from the virtual Argo floats with the "true" values from the model output. We find that although errors in all three quantities decrease with increasing temporal sampling rate, number of floats and experiment duration, the error approaches an asymptotic limit. Thus, as these parameters exceed this limit, only marginal reductions in the error are observed. The parameters of the real Argo array, when scaled to match those of the virtual Argo array, generally fall near to, or within, the asymptotic region. Using the numerical model, a method for the calculation of cross-stream heat-fluxes is demonstrated. This methodology is then applied to 5 years of Argo derived velocities using the ANDRO dataset of Ollitrault & Rannou (2013) in order to estimate the eddy heat flux at 1000m depth across the Polar Front in the Southern Ocean. The heat-flux is concentrated in regions downstream of large

*Corresponding Author
Email address: `chris.chapman.28gmail.com` (Christopher Chapman)

bathymetric features, consistent with the results of previous studies. 2±0.5TW of heat transport across the Polar Front at this depth is found, with more than 90% of that total concentrated in less than 20% of the total longitudes spanned by the front. Finally, the implications of this work for monitoring the ocean climate are discussed.

Keywords: Lagrangian floats, Southern Ocean, Idealized Modelling.

1. Introduction

Deep drifting floats, such the satellite tracked Argo floats and the Autonomous Lagrangian Circulation Explorer (ALACE) floats, or acoustically tracked Sound Fixing and Ranging (SOFAR) and RAFOS floats, provide direct measurements of the oceanic currents as they move with the flow. These floats provide the only direct measurements of the ocean's subsurface currents with broad spatial coverage and have been instrumental in shaping our comprehension of the structure of the ocean's interior (Roemmich et al., 2009; Riser et al., 2016). They have been shown to be capable of producing accurate and rich maps of the time mean interior currents (Davis, 1991a; Gille, 2003a; LaCasce, 2008; Ollitrault and Colin de Verdiére, 2014) and measurements of features not readily inferred from remotely sensed surface measurements, such as deep jets and boundary currents (Richardson and Fratantoni, 1999; Fratantoni and Richardson, 1999; van Sebille et al., 2011, 2012). With the continued development of the Argo program, and the improved geographical and temporal coverage of the global ocean that comes with it, it is reasonable to ask: are we capable of observing robust, quantitative statistics of the oceanic meso-scale with current float deployments?

As a way of introducing the problem, Fig. 1a shows all Argo float positions in the Southern Ocean (south of 30°S) within 5 days of the 25th of December 2009. We have determined the mean distance between each of the points plotted in Fig. 1a and their closest neighbor is approximately 160km. Fig. 1b shows the trajectory of a single float, (World Meteorological Organization number

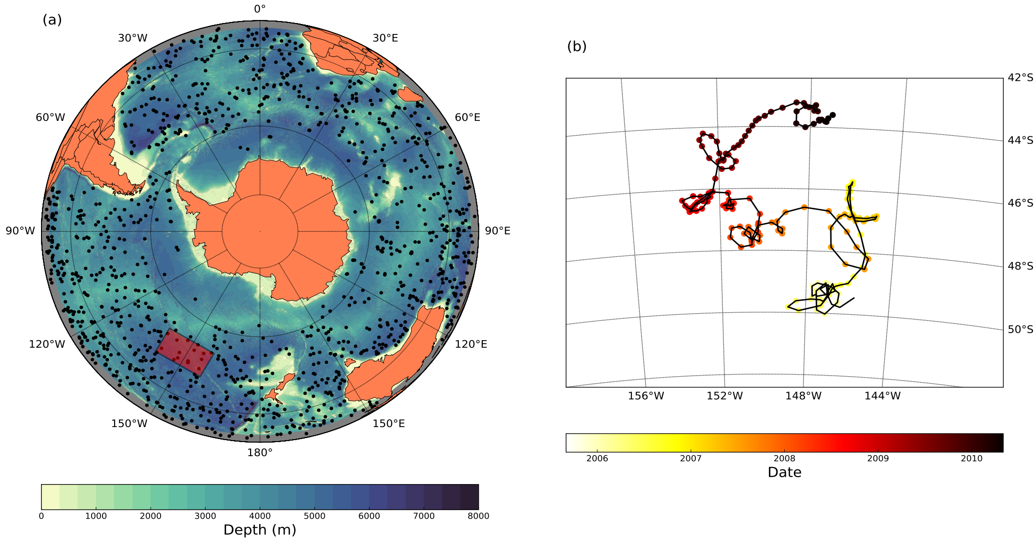

Figure 1: Spatial coverage of Argo floats in the Southern Ocean. (a) All reported Argo float positions at 1000db, within 5 days of the 25th of December, 2009 (points), overlayed over the topography from the ETOPO01 dataset (colored contours); (b) zoom on the highlighted region in panel (a), showing the trajectory of float # 5900777 from the 26th of April 2005 to the 26th of December 2009.

#5900777) over its lifetime. Numerous scales of motion are present in this trajectory, from very tight loops with a radius of order a few kilometers, to larger meanders with a effective radius of several hundred kilometers. The time series of float position is *non-stationary* (that is, the statistical properties of the motion change with time) and, although the Argo float has remained operational for approximately four years, the trajectory is limited to a relatively small part of the ocean, drifting only a few degrees throughout its operational life. As such, this float has repeatedly sampled the same geographic region.

Clearly, Argo float #5900777 'sees' a number of features important to general circulation, including mesoscale eddies superimposed over a larger scale flow field. However, the geographic region sampled by this float is limited. Thus, we pose the question: what characteristic must an array of these floats have in order to resolve the oceanic meso-scale?

Argo floats, by their design, present several challenges for the accurate measurements of deep currents. Argo floats must resurface to transmit their data, leaving the currents inferred from their displacement subject to errors such as delays in the surface location fix, shear in the water column and surface drift (Ollitrault and Rannou, 2013). Although a substantial amount of work has been undertaken to determine and control these errors in the measurement, less work has been devoted to understanding the limitations of sampling and the sampling density, particularly when compared with the large amount of work undertaken to understand the limitations of the surface drifter array (Davis, 1982, 1987, 1991a,b; LaCasce, 2008). Surface drifters and Argo floats have several substantial differences in their sampling characteristics. Due to the fact that surface drifters do not need to complete a dive cycle, they report a position fix every 1-2 hours (Elipot et al., 2016), which is much more frequent than the standard Argo position fixes of once every 5 to 15 days (with the vast majority of floats reporting a position every 10 days). Additionally, the surface drifter dataset has far denser sampling statistics than the Argo array. As such, work performed using surface drifters may not translate directly to Argo floats.

In this study, we use a combined empirical/observational approach to study the influence that sampling, both spatial and temporal, have on the ability to reconstruct deep flows and the eddy fluxes associated with meso-scale motions, treating the Argo float array as a array of "moving current meters" (Davis, 1991b). To do this, we will use a an idealized Observing System Simulation Experiment (OSSE). OSSEs have become relatively common in climate science since the 1980s (Hoffman and Atlas, 2016). The basic principle of an OSSE, described in Hoffman and Atlas (2016), is to take the the output of a numerical model as the "truth" and then sample this output with synthetic observations. With the luxury of knowing the "truth" from the numerical model, the utility of synthetic observing system can then be rigorously evaluated.

We will study the errors associated with the length of time between dive and resurfacing of the floats, the spatial density of the Lagrangian array and the duration of the float experiment will be in place by systematically modifying the density and time span of the virtual float array, as well as the sampling characteristics of the float derived velocities. Specifically, an idealized, eddy resolving numerical model of the Southern Ocean is "observed" using "virtual" Argo floats. By comparing the Lagrangian derived estimates of mean velocity, eddy kinetic energy and heat flux to the "exact" results from the model solution, we will demonstrate the utility and shortcomings of these Lagrangian measurements. We will then use the understanding of the limitations of the Lagrangian derived velocities gained from the model output in order to estimate the eddy heat flux in the Southern Ocean from the existing array of Argo floats. We limit our focus to the Southern Ocean for two primary reason: it is the principle region of study for both authors of this paper; and the lack of available "traditional" observations from ships means that a detailed investigation of the Argo floats' capacity to resolve meso-scale statistics is warranted. However, the results obtained here are expected to apply quite generally.

The capacity of the Argo array to effectively represent important oceanic variables, including current velocity, has already been subject to several OSSEs. For example, Kamenkovich et al. (2011) used a "virtual" Argo float array, designed to resemble the Argo array as it was at the time of publication, to sample the output of a numerical model of the North Atlantic. The virtual Argo float array performance was assessed in two model configurations: with and without mesoscale variability present. Kamenkovich et al. (2009) and Kamenkovich et al. (2011) found that the presence of mesoscale eddies had a profound effect on the virtual Argo array's data coverage, as eddies tend to efficiently disperse floats, leading to broader spatial coverage. Puzzlingly, they find that poor data coverage is not consistently correlated with high reconstruction errors. In contrast, errors are generally higher in regions dominated by strong advection, such as the western boundary currents and the ACC. Focusing on the Southern Ocean, Majkut et al. (2014) used a virtual array of Argo floats equipped with biogeochemical sensors sampling output from the GFDL-ESM2M climate model to demonstrate the potential for these floats to provide useful data from the real ocean, and to suggest sampling strategies for future deployments. Roach et al. (2016) used virtual Argo and RAFOS arrays, advected in the data assimilating Southern Ocean State Estimate (SOSE) model to assess the fidelity of estimates of lateral diffusivity calculated with the real Argo array. However, to our knowledge, no study has investigated the influence of float sampling, array density or experiment time-span on the resulting reconstruction error, nor have the capacity of Argo floats to estimate quadratic quantities, such as heat flux, been rigorously assessed. In this paper it is our intention address these topics.

The remainder of this article is organized as follows: Section 2 discusses the spatial and temporal sampling characteristics of Argo floats and the effects of each on the estimation of underlying flow fields. The numerical model configuration and the method of advecting virtual Argo floats, as wll as the observational datasets that will be used in the second part of this study will be described in Section 3. We will discuss the reconstruction of the numerical model fields from the virtual Argo floats in section 4, and the ability of Lagrangian observations to determine cross-frontal heat fluxes in the numerical model in section 5. Estimates of the mean flow and the cross-stream eddy heat-flux in the Southern Ocean using the Argo float array will be presented in section 6, and the results obtained will be discussed with reference to the numerical model results in section 7.

2. Sampling and Lagrangian Drifters

Here we briefly review the role of discrete sampling in reconstructing real-world signals, and its application to extracting information from Lagrangian drifters.

2.1. Temporal Sampling and Lagrangian Drifters

The position of an idealized Lagrangian float, $\mathbf{x} = (x(t), y(t), z(t))$, is related to the oceanic current velocity $\mathbf{u}(\mathbf{x}; t)$, by:

$$\dot{\mathbf{x}} = \mathbf{u}(\mathbf{x}; t). \quad (1)$$

However, due to their dive, drift and resurface cycle, Argo floats are sampled at discreet time intervals. To determine the current velocity from the Lagrangian measurements, for the mth float cycle, we follow Lebedev et al. (2007) and use the following difference equation:

$$\mathbf{u}^m \left(\mathbf{x}_{\text{deep}}, p_{\text{park}}; t^m_{\text{deep}}\right) = \frac{\mathbf{x}(t^m_{\text{asc}}) - \mathbf{x}(t^m_{\text{des}})}{t^m_{\text{asc}} - t^m_{\text{des}}} \tag{2}$$

where $\mathbf{x}_{\text{deep}}$, t_{deep} and p_{park} are location, time and parking pressure of the deep velocity estimate, $\mathbf{x}(t_{\text{asc}})$ and t_{asc} are the location and time of the float ascension; and $\mathbf{x}(t_{\text{des}})$ and t_{des} are the location and time of the float descent for that cycle. For the majority of Argo floats, the parking pressure is approximately 1000db. If the time between ascent and descent, Δt, remains constant over the lifetime of the float (which is true for the virtual floats by construction, and approximately true of Argo floats), and if the descent time of cycle $m+1$ is equal to the ascent time of cycle m, then Eqn. 3 can be written:

$$\mathbf{u}^{m+1/2} \left(\mathbf{x}^{m+1/2}, p_{\text{park}}; t^{m+1/2}\right) = \frac{\mathbf{x}^{m+1} - \mathbf{x}^m}{\Delta t}. \tag{3}$$

where $m+1/2$ represents some time between cycles m and $m+1$.

Eqns. 2 and 3 clearly represent a discreet approximation of the continuous circulation. This discretisation process induces both a truncation error, which is $O(\Delta t)$, but also an aliasing error, which occurs as a consequence of sampling with a frequency lower than twice that of the highest frequency present in the underlying flow (Smith, 1997, pgs. 39–44). Treatment of aliasing in Lagrangian measurements is not trivial, as the sampling rate provided by the floats depends on the velocity of the flow being sampled (Willis and Fu, 2008). An example of aliasing of the flow field is shown in Fig. 2, which compares the velocity obtained from a Lagrangian drifter using higher (red arrows) and lower (blue arrows) sampling rates. It is clear from Fig. 2 that a low sampling rate yields a velocity estimate that does not capture the structure of the underlying flow field, nor give an accurate velocity estimate. This picture is further complicated by the fact that if the velocity of the flow were to increase, then the Lagrangian float would be advected through the flow structure more rapidly, and the spatial

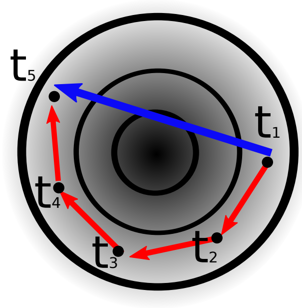

Figure 2: Schematic showing the aliasing of float observations. The shaded background and black, solid contours show the streamfunction of an idealised anticyclonic eddy. The black dots represent the float location at 5 seperate times. The red arrows represent the velocity observations determined at the highest availble sampling rate: $\Delta t = t_2 - t_1, t_3 - t_2, \ldots$. The blue arrow represents velocity estimate made by sampling only the first and last float positions: $\delta t = t_5 - t_1$.

sampling would change in response.

In this paper we make no attempt to tease out the individual influences of aliasing and truncation on the overall error performance. Instead, we treat these two sources of error together as a 'temporal sampling error' and note that the truncation error is expected to grow linearly with Δt. The aliasing error is expected to be non-stationary: larger in regions dominated by intense features such as eddies are jets. We will explore how the background flow field modifies the error obtained using Lagrangian measurement in section 4.

2.2. Spatial Sampling provided by Argo floats in the Southern Ocean

Fig. 3 gives an indication of the geographical coverage provided by the dataset in the Southern Ocean. Fig. 3a shows the average number of observations south of 40°S, binned by longitude and latitude with a bin size of $1° \times 1°$, between 2005 and 2011 (the time span of the ANDRO dataset). Throughout most of the Southern Ocean, the density of observations relatively homogeneous. However, there is a rapid reduction in data availability in high latitudes. Fortunately, regions with limited observational density typical occur south of the main ACC fronts (compare Fig. 3a with Fig. 14 or Fig. 4 of Dufour et al.

(2015)) and, as such, the ACC region which is the principle focus of this study, can be considered to be approximately evenly sampled by the Argo floats.

To further understand the distribution of Argo based observations in the Southern Ocean, we now plot the total number of observations south of 40°S, binned by longitude with a 1° bin size, in Fig. 3b (black line). The number of observations is spatially variable, with a minimum in Drake Passage longitudes (70°W to 60°W) of approximately 50 observations per degree of longitude over the 5 year period, and a maximum of approximately 450 observations per degree located upstream of Drake Passage at ∼90°W. An average of 220 observations are taken in each longitude bin over the 2005-2011 period. Fig. 3b also shows the average number of floats in each longitude during a 10 day window (red line), which gives an approximation of how many simultaneous measurements are taken in each "snapshot". The curve in Fig. 3b broadly follows than of 3a, with peaks and troughs in roughly the same longitudes. The average number of floats available in a 10 day period over the entire Southern Ocean basin is 400±30.

The preceding analysis demonstrates that the data coverage provided by Argo floats in the Southern Ocean is spatially variable, and that there are frequently no Argo floats available to sample a particular region. With an average distance between 'simultaneous' measurements of ∼160 km in the Southern Ocean, which is an order of magnitude greater than the local Rossby deformation radius, resolution of the instantaneous mesoscale field is impossible using Argo floats. However, given that certain floats repeatedly sample the same region and even the same feature (see Fig. 1b) it is difficult to infer a spatial resolution from float distributions alone. Indeed in a similar OSSE Kamenkovich et al. (2011) found only a weak correlation between the how well sampled a region was and the underlying error of the reconstruction. How well the mesoscale statistics are represented with the existing Argo array, and how their representation changes with variations in array parameters, such as the number of floats and the length of time of the float experiment, is the focus of the remainder of this paper.

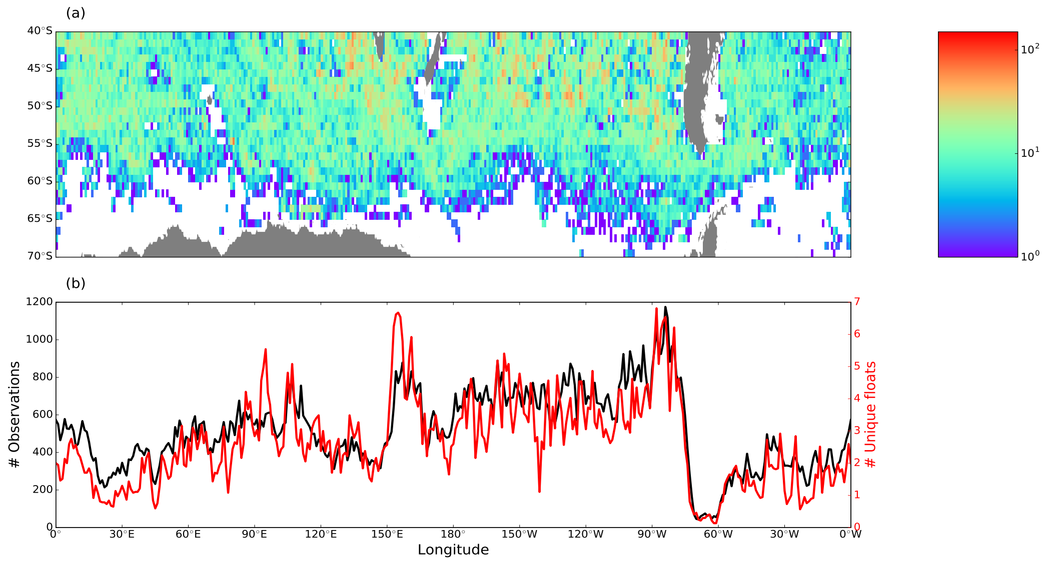

Figure 3: The Argo array spatial sampling characteristics in the Southern Ocean: (a) The number of velocity observations, between 2005 and 2010, south of 40° at 1000m depth, binned onto a 1° longitude/latitude lgrid; and (b) the total number of velocity observations south of 40° in each 1° longitude bin, across all latitudes (black) and the average number of individual Argo floats availble in a 10 day "snapshot" period, in each 1° longitude bin (red).

3. Numerical Model, Argo Data, and Methods

In this section, we will introduce our idealized numerical model and our method of advecting numerical ('virtual') Argo floats. We will also describe the observational Argo float dataset (the ANDRO dataset) from which we will reconstruct the mean and eddy fluxes.

3.1. Numerical Model Configuration

The configuration of our numerical model is an idealized representation of the Southern Ocean, inspired by Abernathey et al. (2011). Here, we use the Nucleus for European Modelling of the Ocean (NEMO) model, version 3.6 (Madec, 2014), which solves the three-dimensional primitive equations on the β-plane, in standard vertical depth coordinates, using a C-grid for the spatial discretization and a linear equation of state with a constant salinity of 25 g.kg^{-1}. Our configuration is a zonally periodic Cartesian channel with a zonal length, L_x of 6000km and a meridional width, L_y of 2000km and a maximum depth H of 4000m. Advection of both momentum and tracers is handled by the 3rd order upwind-biased scheme, which induces a resolution dependent implicit diffusion. Thus, no explicit horizontal diffusion or viscosity is applied. Vertical diffusion is handled using a Generic Length Scale (GLS) scheme. Surface forcing is supplied by a meridionally varying sinusoidal wind-stress $\tau(y) = \tau_0 \sin(\pi y/Ly)$ and by relaxing the surface to an imposed linear surface temperature distribution, with a relaxation coefficients of 30W.m^{-2}K^{-1}, as in Barnier et al. (1995). Additionally, following Abernathey et al. (2011) the temperature on the northern 150km of the domain is relaxed to an exponential temperature profile, with a relaxation coefficient of 7 days^{-1}, which allows for the formation of a residual overturning.

We induce zonal assymetry in the model by the introduction of bottom bathymetry. As in Abernathey and Cessi (2014), we use a meridional ridge with a Gaussian cross-section described by:

$$h(x) = H_0 e^{\frac{-(x-L_x/2)^2}{\sigma_0^2}},$$

where h is the height of the bathymetry above the ocean floor, x is the zonal coordinate, σ_0=150km is the topographic length scale and $H_0 = 2000m$ is the scale height of the topographic obstacle. The scale height and topographic length scales has been chosen to effectively block lower layer flow and induce a large stationary meander, thus effectively capturing some of the impacts of large bathymetric features, such as the Kerguelen Plateau, on the Southern Ocean circulation.

The model horizontal grid spacing is 5km and 50 vertical levels, distributed such that the vertical grid spacing is smaller towards the surface and deeper towards the ocean floor (minimum Δz of $\sim$5m, maximum of $\sim$175m). With an

Table 1: Parameter values used in the configuration of the numerical model.

Symbol	Value	Description
L_x	6000km	Zonal Domain Length
L_y	2000km	Meridional Domain Length
Δx, Δy	5km	grid-spacing
Δt	300s	barotropic time-step
H	4000m	Depth
H_0	2000m	Topography Scale Height
f_0	$-1.0\times10{-}4\text{s}^{-1}$	Coriolis parameter
β	$1\times10^{-11}\text{s}^{-1}\text{m}^{-1}$	Meridional
τ_0	$1.5\times10^{-4}\text{N.m}^{-2}$	Peak wind stress
r_D	$1.5\times10^{-3}\text{m.s}^{-1}$	Linear bottom drag
κ_v	$0.5\times10^{-5}\text{m.s}^{-2}$	Vertical diffusivity
T_S	7 days^{-1}	Sponge layer relaxation time-scale
α	2.0×10^{-4}	Thermal expansion coefficient
g	$30\text{W.m}^{-2}\text{K}^{-1}$	Surface temperature relaxation coefficient

approximate Rossby deformation radius of 20km (verified by direct calculation after spin-up), this grid spacing is sufficient to explicitly resolve the meso-scale. The model is spun-up for 200 years, which is sufficient for the interior flow to attain statistical equilibrium, and then run for an additional 10 years. We output the snapshots of the model velocity (u, v, and w components) with daily temporal frequency. Additional parameter choices are noted in Table 1.

An example of the model output at 1000m depth is shown in Fig. 4. Fig. 4a shows the time-mean horizontal speed of the simulated currents at 1000m depth. Although highly idealized, our simulation captures a number of phenomena present in the ocean. As in the Southern Ocean, our simulation shows the flow

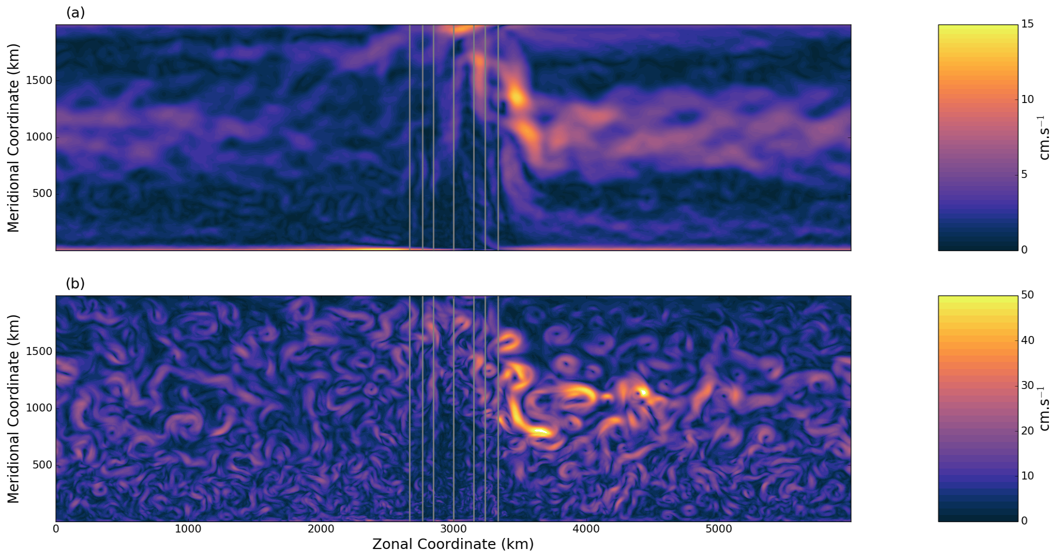

Figure 4: An example of the numerical model output at 1000m depth. (a) The mean current speed, taken over the 10 years of the model run; and (b) a snapshot of the current speed. The solid grey lines indicate the idealised topography depth (CI:500m)

organized into a series of zonal jets. The currents are steered by the bathymetry, being diverted to the north as they traverse the obstacle. Downstream of the bathymetry, a stationary meander is formed. Fig. 4b shows a snapshot of the current velocity at 1000m. Meso-scale features are evident throughout the domain, with an enhanced intensity downstream of the bathymetry, reminiscent of an oceanic storm-track (Williams et al., 2007; Chapman et al., 2015). Characteristic mean velocities are found to be 10–15cm.s^{-1}, with instantaneous velocities that can reach 60cm.s^{-1}, consistent with observations in the Southern Ocean (Ollitrault and Colin de Verdiére, 2014).

3.2. Virtual Argo Float Advection

In this study we shall make extensive use of virtual Argo floats advected by the model fields. Hence, it is worthwhile to briefly discuss the numerical implementation of the particle advection scheme and some of the assumptions behind it.

We solve Eqn. 1 using a 4th order Runge-Kutta scheme with an adaptive time-step, allowing us to specifically control the error of the solution while maintaining computational efficiency. In practice, the truncation error of the solution is required to be less than 10^{-3} (that is one part in 1000), although the true computational error may be less than this value. Floats are advected "offline", using saved model output. The velocity at a particular virtual float time and position is obtained by 3D linear interpolation.

The virtual Argo floats are advected on a constant depth surface: thus, there is no vertical displacement of the particle. Additionally, we do not require our floats to undergo a surfacing/descending 'dive' cycle: the virtual float positions are thus known exactly and there are no errors arising from vertical shear in the water column, nor position fix delays. As such, the virtual Argo floats can be considered to be "perfect" q in the sense that the only source of error is numerical. Roach et al. (2016) have tested how the Argo dive cycle affects the estimations of diffusivity when compared to 'perfect' virtual floats in a realistic numerical simulation of the Southern Ocean. They found that, even with relatively pessimistic assumptions, the Argo dive cycle induced errors that were small relative to natural variability within the ocean. Although this calculation was performed in a different context, the results obtained by Roach et al. (2016) allow us to assume that neglecting the Argo dive cycle will not significantly affect the resulting reconstructions.

450 virtual Argo floats are advected in the model at a depth of 1000m. The number of floats is selected by noting that there are, on average, 400 $\pm$ 30 floats in the Southern Ocean latitudes south of 40° at any particular time (see Section 2.2). At 55°S, the earth's circumference is $\sim 22\times10^3$km, resulting in $\sim$0.02 floats per kilometer of zonal extent. With the model zonal basin length of L_x =6000 km, 110$\pm$10 floats are required in the model to maintain an equivalent number of floats per degree of longitude in the model. To test how the reconstruction error changes with additional floats, we use 4 times the minimal

number floats required, hence 450. The location of each virtual float is saved daily: thus there are 3650 x and y position records (10 years × 365 days/year) for each of the 450 floats in the experiment, giving a total of 1,642,500 virtual float positions.

It is important to note that even with the relatively high rate at which the model output is produced (1 day) the virtual Argo floats are liable to 'overshoot' (Keating et al., 2011) due to unresolved high frequency motions. Following Keating et al. (2011), we have attempted reduce this error by maintaining a maximum time step in the virtual Argo float integration of $\Delta t = 1$ hour and linearly interpolating the model fields (both spatially and temporally) to the virtual float location. At 5km grid spacing, this places our float experiment within the 'overshoot' regime (see Fig. 14 of Keating et al. (2011)). However, as noted by Keating et al. (2011) interpolation cannot eliminate the problem of particle overshoot, and, as such, it is likely that our virtual particles show spuriously high diffusivity due to this numerical effect.

3.3. Deep Current Velocities, and Temperature and Salinity Profiles From Argo Floats

For the observational component of this study, we make use of the ANDRO dataset (Ollitrault and Rannou, 2013), freely available for download (http://wwz.ifremer.fr/lpo/). ANDRO provides estimates of the current velocity at the parking pressure of the float and at locations that are estimated from the locations of the previous two surface locations estimates, while controlling for, or estimating, sources of error such as those due to vertical shear, surface fix delay, surface drift due to inertial oscillations and uncertainty in the dive time. Unlike similar datasets (for example the YoMaHa'07 dataset of Lebedev et al. (2007)) ANDRO also explicitly accounts for drift in the parking pressure that occur over the lifetime of the float. We consider floats between the years 2005 and 2011. A total of 2440 floats are available south of 10°S, yielding a total of 217,065 independent estimates of velocity at depths ranging from 500db to 2000db, although in practice, we consider only velocity estimates near 1000db.

In section 6 of this paper, we will estimate the heat fluxes using Argo data. As such, knowledge of the temperature at the float parking depth is required. We obtain profiles of temperature, salinity and pressure from the surface to 2000db, for each of the floats in the ANDRO database from the various Argo Global Data Assembly Centers (Roemmich et al., 2009; Riser et al., 2016). The temperature and salinity are then used to determine the conservative temperature T using the TEOS-10 algorithm (McDougall and Barker, 2011). The value of T is then interpolated to the ANDRO velocity data locations using linear interpolation from adjacent float locations as in Elipot et al. (2016).

3.4. Reconstruction of Fields from Point Observations

The data provided by Lagrangian float observations are scattered and unstructured. As such, in order to estimate oceanographic fields on a regular grid, some mapping or 'interpolation' scheme must be employed. In most of the oceanographic literature, mapping is accomplished by optimal interpolation (Wunch, 2006, p. 163) or local least-squares fitting (Ridgway et al., 2002). Although powerful, these methods are computationally intensive. Since we will be performing numerous reconstructions, we chose to use the simpler procedure of geographic binning (Davis, 1991b; LaCasce, 2008). With this methodology, the domain is discreetized into $N_x \times N_y$ points. All observations of some quantity, θ, that fall within some radius, R, of a particular grid point, are averaged to form a local ensemble mean:

$$\overline{\theta}(\mathbf{x}_i) = \sum_{d_{ij}<R} \theta_k(\mathbf{x}_j; t_j), \tag{4}$$

where d_{ij} is the distance from the grid-point $\mathbf{x}_i$ to the float location $\mathbf{x}_j$. The geographical binning approach makes the implicit assumption that the mean and any residuals have distinctly different time scales, that there are sufficient observations to reliably estimate the mean, and that the binning radius, R is less than the decorrelation scale of the underlying data (LaCasce, 2008). Even assuming that these conditions have been met, geographic binning has numerous shortcomings. For example, the choice of radius R can influence the spatial scale of the reconstructed flow. In addition, in situations where the number of Lagrangian observations is variable in space, random background processes can give rise to a spurious velocity down the gradient of the observational sampling density (that is, the number of samples per unit area) (Davis, 1991b). In principle, it is possible to correct for this effect, although it is technically difficult (Davis, 1991b, 1998).

Despite these problems, we persist with this methodology due to its computational speed and since we are principally interested not in the absolute error of the reconstruction, but instead the *relative errors* over the parameter space to be explored. However, the reader should keep in mind the shortcomings of the mapping procedure and recognize that absolute errors in fields produced in this paper can be considered a "worst case" scenario and could be improved through the application of more sophisticated methods.

4. Reconstruction of Mean and Eddy Fields in the Idealized Model

We now study the ability of velocities inferred from Lagrangian displacement data to effectively reconstruct the large-scale flow field and the statistics of the meso-scale using the virtual Argo floats advected in the numerical model. We will test the sensitivity of the reconstruction to the number of virtual floats, the length of time of the float experiment and their sampling characteristics. On first glance, varying the number of floats and the length of time of the experiment may seem redundant, as each parameter simply modifies the number of observations. However, Argo floats are costly, and the absolute number of Argo floats in the ocean is not expected to substantially increase in the next few years, although there may be an increased focus of increasing the density of observations selectively in certain regions (Riser et al., 2016). Additionally, the number of floats must be sufficient to sample the majority of the domain. A single float, for example, is unlikely to sample the entire model domain unless the experiment is run for a prohibitively long time. As such, since number of Argo floats is expected to remain somewhat fixed, it is certainly worth considering how the fidelity of the reconstruction will change should the Argo array continue to operate with an unchanged number of floats.

4.1. Instantaneous Errors and the Effects of Temporal Sampling

In order to test the influence of the temporal sampling on the velocity errors, we determine the virtual float velocities using sampling periods of every 1, 2, 5, 10, 20, 30, 40 and 50 days. In order to simulate the effects changing the temporal sampling rate, Eqn. 3 is modified to include the sampling interval, $K \in \mathbb{Z}$:

$$\mathbf{u}^{m+K/2}\left(\mathbf{x}^{m+K/2}, p_{\text{park}}; t^{m+K/2}\right) = \frac{\mathbf{x}^{m+K} - \mathbf{x}^{m}}{t^{m+K} - t^{m}} = \frac{\mathbf{x}^{m+K} - \mathbf{x}^{m}}{K\Delta t}. \quad (5)$$

By calculating the Lagrangian velocities in this manner, rather than simply sub-sampling the Lagrangian time series, the total number of velocity remains approximately constant, which avoids the problem of reducing the number of samples in the signal that would occur if it were sub-sampled naïvely. We note, that each virtual Argo float trajectory must be truncated by $K-1$ points due to the finite length of the rolling window, although since the number of observation removed is small compared to the total number of observation the truncation has no discernible effect on the resulting statistics. In this section we use 110 virtual floats, which is the number of virtual floats required to ensure that the number of floats per degree of longitude in the model is representative of the Argo array in the ACC.

The normalized histograms of the u and v velocity estimated from the virtual floats is shown in Fig. 5, where they are compared with the distributions calculated directly from the model output (thick black dashed line). Although the estimated distributions show a similar Gaussian character to the true distribution, the virtual floats tend to produce distributions that underestimate the frequency of large magnitude velocities, as the tail of the estimated distributions fall below that of the true distribution for velocities with magnitudes larger than $\sim$7.5cm.s^{-1}. As such, the virtual Argo floats tend to underestimate the magnitude of more extreme velocities produced by the model. Additionally, the estimated distributions also tend to differ from the true distribution when velocities are weak. At high sampling rates, the velocity obtained from the virtual Argo floats tends to *underestimate* the frequency of weak velocities when the sampling rates are high (1–10 days), and *overestimate* their frequency when the sampling rates are low (20–50 days). There is also a significant asymmetry in the distribution of v that is most notable at strongly negative values. We are unable to definitively identify the cause of this asymmetry, although we speculate that if may arise due to the fact that the storm track region, where the strongest eddy velocities are found, is collocated with strong southward mean flow induced by the stationary meander. We note also that the virtual argo floats are not able to capture this asymmetry, consistent with their underestimation of the true flow velocity in the tails of the distribution.

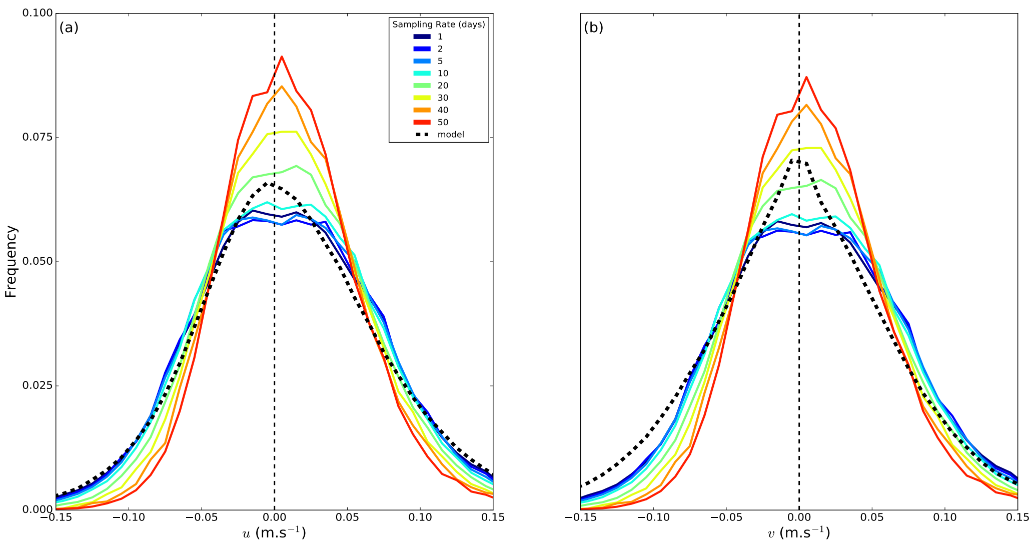

Figure 5: The normalized histograms for the zonal (a) and meridional (b) current velocities estimated by the virtual Argo floats, for each temporal sampling interval (see legend in panel (a)). The histogram computed directly from the model output at each of the float sampling points is indicated by the thick, dashed black curve.

To further explore the ability of the virtual Argo floats to estimate the modeled currents, at the location of each virtual float velocity measurement, we calculate the absolute velocity error:

$$\epsilon_{\mathbf{u}}^{\text{abs}}(\mathbf{x}_i;t) = \hat{\mathbf{u}}(\mathbf{x}_i;t) - \mathbf{u}(\mathbf{x}_i;t), \tag{6}$$

and the relative velocity error:

$$\epsilon_{\mathbf{u}}^{\text{abs}}(\mathbf{x}_i;t) = \frac{\hat{\mathbf{u}}(\mathbf{x}_i;t) - \mathbf{u}(\mathbf{x}_i;t)}{\mathbf{u}(\mathbf{x}_i;t)} \tag{7}$$

where $\hat{\mathbf{u}}(\mathbf{x}_i;t)$ is the velocity estimated from the virtual Argo floats and $\mathbf{u}(\mathbf{x}_i;t)$ is the "true" velocity taken directly from the model at virtual float location $\mathbf{x}_i \forall i \in \left[1, N_{\text{obs}}\right]$, which is estimated at the virtual float locations by bilinear interpolation. These error estimates are averaged meridionally and binned by longitude with a bin size of 20km (4 grid cells). We have tested bin sizes from 10km to 50km, and found 20km to be a good compromise between the smoothness of the reconstructed fields and the ability of the our methodology to reconstruct important features. In each longitude bin, we compute the root-mean-squared-error:

$$\text{RMSE}_{\mathbf{u}}^{\text{abs,rel}} = \left[\frac{1}{M}\sum_{i\in\mathcal{B}}^{M}\left(\epsilon_{\mathbf{u}}^{\text{abs,rel}}(\mathbf{x_i};t)\right)^2\right]^{1/2} \tag{8}$$

where M is the number of observations in each longitude bin and $\mathcal{B}$ represents the current longitude bin.

Fig. 6a shows the RMS of the absolute meridional velocity error ϵ_v^{abs} in each longitude bin (the zonal component shows very similar behavior). It is clear that the absolute error in the velocity estimated by the virtual floats, regardless of the sampling rate, increases downstream of the bathymetry (indicated by the dashed line in Fig. 6a). It is in the downstream "storm track" region that mesoscale eddies are the most intense (Chapman et al., 2015). The velocity error shows the greatest sensitivity to the sampling rate in the storm track. In the region upstream of the obstacle, the difference between the velocity estimates obtained using a sampling rate of 1 day and 50 days is approximately 5cm/s in the less energetic upstream region, while the difference in errors increases to 1.25cm/s in the energetic storm track region. However, it is worth noting that the difference between errors obtained using a sampling rate of 1 day and those using a sampling rate of 10 days (the usual Argo sampling frequency) are indistinguishable upstream of the topopgraphy and the difference is limited to less than 2.5cm/s even in the storm track region. The virtual Argo floats are able to estimate the current speed with RMS errors of approximately 2.5cm/s upstream of the topography and approximately 5cm/s in the region downstream of the topography when the sampling rate is 10 days or less.

Investigation of the relative errors, plotted in Fig. 6b, reveals that the virtual Argo floats have errors between 20% with sampling periods less than 20 days, rising to errors that are 80-100% for sampling rates of once every 50 days. In contrast to the absolute errors, the relative error remains approximately constant throughout the domain for sampling rates more frequent than 20 days. For sampling rates more frequent than 20 days, the relative error in the velocity increases by approximately 20% in the storm track region. Since velocities are highest in the turbulent region downstream of the topography, the relative insensitivity of the relative error throughout the domain underscores the strong dependence of the instantaneous error on the velocity being observed.

Fig. 6 also shows the distributions of $\epsilon_{\mathbf{u}}$ for both the zonal (Fig. 6c) and meridional (Fig. 6d) components. The distributions for each velocity component are very similar, save for asymmetry that is present in the zonal error distribution. With changing sampling rate, both ϵ_u and ϵ_v distributions show a decreasing frequency of errors near zero and increasing standard deviation with increasing sampling period.

To understand how velocity errors manifest it is instructive to examine the scatter between the virtual Argo float velocity error and the true velocity, as in Fig. 7a for sampling rates of 1, 10 and 50 days for the v velocity component (the u component has a similar structure). Fig. 7a shows that, for all cases considered, there is a significant negative correlation between ϵ_v and the velocity being measured. As such, the virtual Argo floats tend to *underestimate* strongly

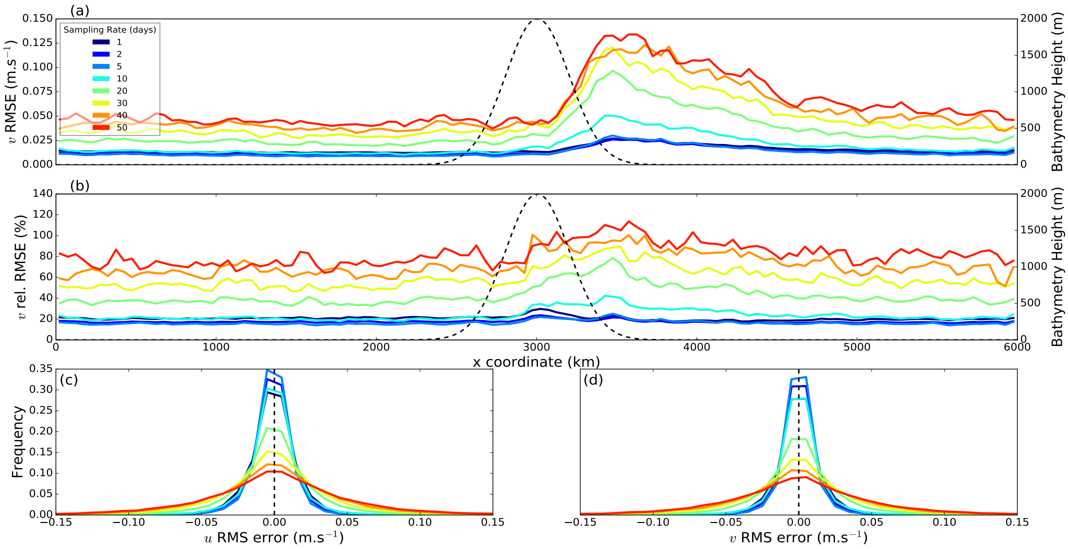

Figure 6: The effect of temporal sampling on the error in the velocity. (a) The *absolute* RMS errors in v, defined in equation 8 binned by longitude with a bin size 20km and averaged between y =500km and 1500km for each temporal sampling interval (colors) and; (b) as in panel (a) but for the the *relative* RMS errors in v. The thin dashed line indicates the topopgaphy height. The (normalised) histogram of the errors in the u (c) and v (d), for each temporal sampling interval (see legend in panel (a)).

positive velocities and *overestimate* strongly negative velocities. A linear fit for each sampling rate is obtained using orthogonal regression (used in lieu of standard linear regression due to the increased density of points clustered near 0), plotted in Fig. 7a (dashed black line) for the 10 day sampling rate. The slope of this linear fits is negative for all sampling rates more frequent than 30 days, suggesting a consistent underestimation of high current speeds even at relatively high sampling rates. The scatter of points away from the best fit line increases as the sampling rate is decreased, particularly around 0m/s. In fact, with a sampling rate of 1 day, the points in Fig. 7 cluster about 0, giving the impression of data "funnelling" towards the axes center. For the 10 day sampling period, the scatter of the error remains approximately constant about the best-fit line, while for the 50 day sampling, the error performance for slower current velocities (near v=0) deteriorates.

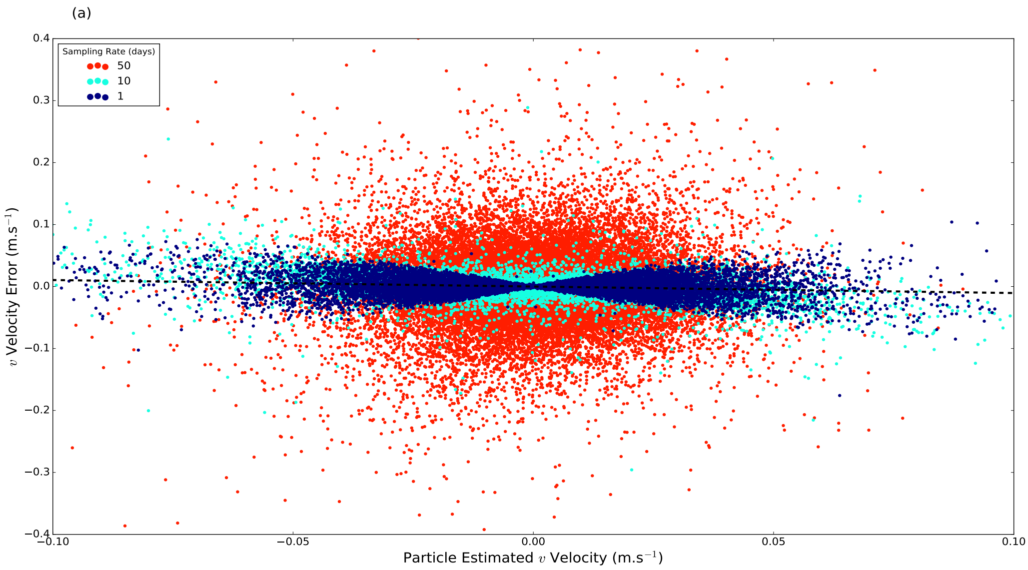

Figure 7: Influence of the current speed on the error. Velocity error (ordinate) vs. the estimated velocity (abscissa) for temporal sampling intervals 1 day (red), 10 days (turquoise) and 50 days (blue). The dashed line indicates the linear fit for the 10 day sampling period (slope -0.3m.s^{-1}/m.s^{-1}).

Are the virtual floats able to capture the dominant spatial and temporal scales of variability present in the model? Directly relating Lagrangian measurements to Eulerian is a complex task beyond the scope of this article, as a Lagrangian drifter moving through a flow field observes both spatial and temporal variations simultaneously (Middleton, 1985; Maas, 1989; Rupolo et al., 1996; Rupolo, 2007). However, we note that by assuming that the turbulence field evolves slowly on the advective time-scale (which is Taylor's "frozen field" hypothesis), then Eulerian wavenumber (spatial) and frequency (temporal) spectrum should have the same slopes (Taylor, 1938; Arbic et al., 2012). As such, if the frozen field hypotheis holds, and we should note that there is now substantial evidence that this hypothesis is only partially applicable to geostrophic turbulence (Arbic et al., 2012, 2014), if we are able to estimate the local Eulerian frequency spectrum from the Lagrangian observations, then we should also be able to develop qualitative understanding of the distribution of local spatial scales.

Middleton (1985) and Maas (1989) have shown that frequency spectra of Lagrangian observation will approximate the Eulerian frequency spectra when averaged over an ensemble of Lagrangian observations. Maas (1989) also showed that the Lagrangian spectra of an ensemble of floats well approximates the Eulerian spectra obtained by measurements fixed relative to a moving background flow, although the Lagrangian spectrum is 'smeared' when compared to the Eulerian spectrum. As such, we compute the Fourier transform of the complex velocities:

$$\tilde{v}(t) = u(t) + iv(t), \tag{9}$$

for all virtual floats with segments of at least one year within the two sub-domains shown by the black rectangles in Fig. 9. These sub-domains are chosen to be representative of the two dominant dynamical regimes in the model: energetic storm track region downstream of the topography, and the quieter region upstream of the topography. These individual virtual float spectra are then averaged together and compared with the complex velocity spectra computed directly from the model fields, area averaged over each individual region. The comparison between the PSDs is presented in Fig. 8a for the non-energetic eastern box, and in Fig. 8b for the energetic storm track region (a comparison between the spectra of the two regions is shown in the inset box). Note that as the PSDs are computed from complex time-series, the PSDs are asymmetric. Recall that highest frequency resolvable from discretely sampled observations is half the sampling frequency.

We find that the ensemble average of the virtual float spectra follow closely the area-averaged Eulerian spectra taken directly from the model output. Over comparable frequency ranges there is little difference between the sampling rates. However, the virtual float spectra are generally too steep though the intermediate frequency ranges within in the non-energetic region (Fig. 8b) and over all frequencies higher than about 0.05 days^{-1} ($\sim$20 day periods) in the storm track region, indicating that over the temporal scales that contain some parts of the meso-scale field, some energy is not being captured by the virtual floats.

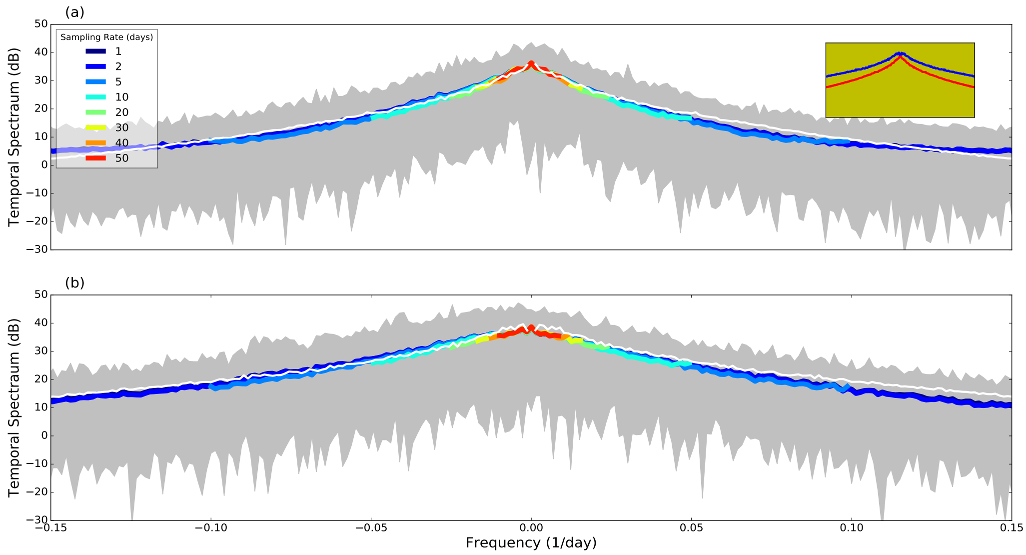

Figure 8: The temporal power spectral density $S(\omega)$ of the complex velocity $w = u + iv$, computed directly from the model output (white lines, inset) compared to ensemble average of all virtual float tracks longer than 1 year (colors) averaged over the (a) western (quiet) box; and (b) eastern (eddying) box. The indivdual colors correspond to velocity data calculated using different sampling frequencies. Grey shading shows the ensemble of float spectra. Note the log-linear axis scale. The inset box in panel (a) shows the average PSD for the western (red) and eastern (blue) regions computed directly from the model.

To summarize the results of this analysis virtual Argo float derived velocities well represent the modelled current velocities and their probability distributions provided that the sampling rate remains more frequent that about 20 days. However, there is a notable tendency for the Lagrangian derived velocities to underestimate the magnitude of the current velocity, particularly as the speed increases, regardless of the sampling rate. The ability of Argo floats to accurately estimate the instantaneous flow velocity will have important implications for the Argo array to effectively determine meso-scale eddy statistics.

4.2. Reconstruction of Mean and Eddy Fields from Lagrangian Observations

We now discuss the problem of reconstructing mean and eddy fields from noisy Lagrangian drifter velocities. We approach the problem empirically, investigating systematically the effects of changing the Lagrangian array parameters on the reconstructed fields.

4.2.1. Effect of Temporal Sampling

As shown in section 4.1, local estimates of the current velocity are sensitive to the temporal sampling rate. As such, we expect that the sampling rate would also affect the ability to reconstruct the large-scale flow fields.

As an example of the reconstruction of the model fields from 110 virtual Argo floats with a 10 days sampling rate (the standard Argo sampling rate) is shown in Fig. 9. For comparative purposes, the model fields are shown in panels (a)i–(c)i, and the equivalent fields reconstructed from the virtual Argo floats in panels (a)ii–(c)ii. We have chosen to investigate the time-mean meridional velocity v, the eddy kinetic energy $EKE = 0.5\left[\overline{u'u'} + \overline{v'v'}\right]$ and the meridional heat flux density $\rho c_p \overline{vT}$. The later two quadratic quantities can give an indication of the ability of the virtual Argo floats to resolve eddy processes.

Fig. 9 shows good qualitative agreement between the model output and the reconstructed fields. The virtual Argo data is able to reproduce the standing wave produced by the interaction of the mean flow with topography, the magnitude and the extent of the storm track produced downstream of the topography, and the response of the meridional heat flux to both. However, there is a tendency for the virtual Argo floats to underestimate these fields, consistent with

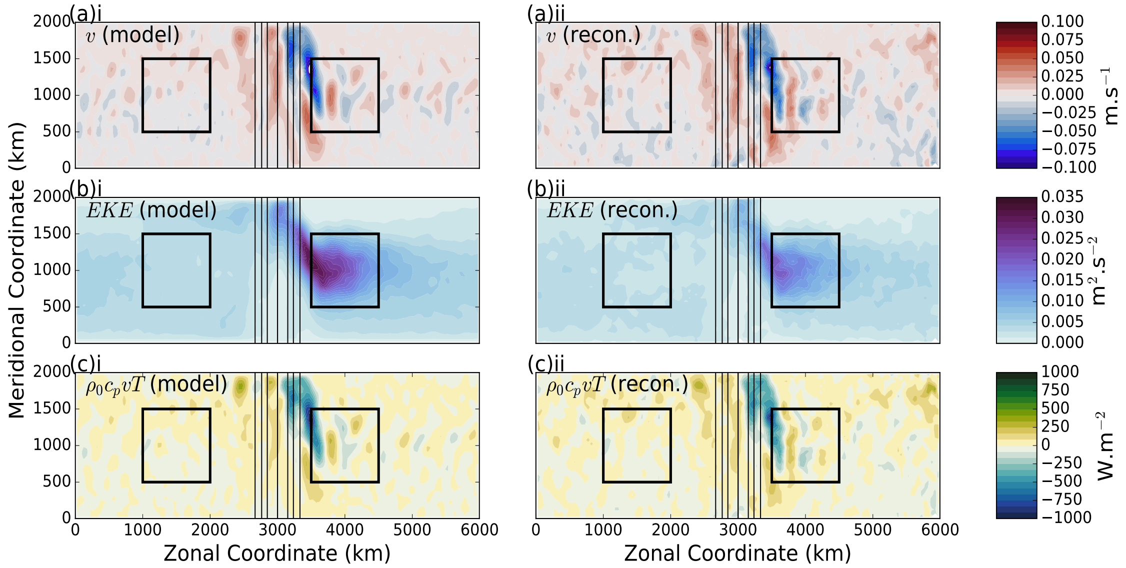

Figure 9: Comparison of the model fields at 1000m vs. fields reconstructed from virtual drifters with a 10 day sampling rate. The modelled (i) and the reconstructed (ii) fields of (a) time mean velocity $\overline{v}$; (b) eddy kinetic energy; and (c) meridional heat flux $\rho_0 c_p \overline{vT}$ Thin black lines are bathymetric contours (CI: 500m) and the thick black lines show the boxes for the proceeding error calculations.

the analysis in section 4.1 which showed an increasing underestimation of the current speed as that speed increases.

To understand more quantitatively the sensitivity of the errors, we compute the RMSE, both absolute and relative of the difference between the true and the reconstructed fields within the two sub-domains shown in Fig. 9. The *absolute* RMSE for an arbitrary time-mean field $\theta(x, y)$ and its reconstruction $\hat{\theta}(x, y)$ is defined as:

$$\text{RMSE}^{\text{abs}} = \left\{ \frac{1}{N_x N_y} \sum_{j}^{N_y} \sum_{i}^{N_x} \left[\hat{\theta}(x_i, y_j) - \theta(x_i, y_j) \right]^2 \right\}^{1/2} \tag{10}$$

where $x_i, y_j \forall (i, j) \in \{(1, \ldots, N_x, 1 \ldots N_y)\}$ are the grid points inside the sub-domain, and N_x and N_y are the total number of grid points in the sub-domain.

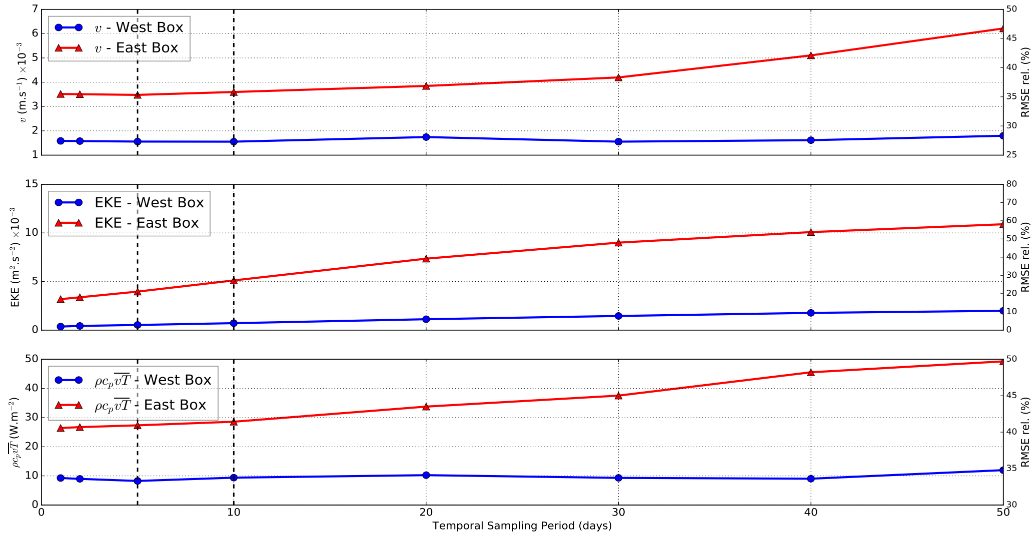

Figure 10: The area averaged RMSE computed over the eastern (blue) and western (red) as a function of sampling interval, Δt for the (a) meridional velocity v; (b) the eddy kinetic energy EKE; and (c) the meridional heat flux $\rho_0 c_p vT$. Dashed black lines indicate the parameter regime occupied by Argo floats.

The *relative* RMSE is the absolute RMSE normalized by the variance of the θ over the sub-domain.

The RMS errors for each of the quantities, integrated over the two subdomains, are shown in Fig. 10. For all quantities considered here, the error is relatively insensitive to changes in the temporal sampling rate in the western (quiet) region (blue line, circular markers). However, in the storm track region (red line, triangular markers) the error shows strong sensitivity to the sampling rate, with a non-linear response that accelerates when Δt increases over about 20 days.

Despite the rapid increasing error with lower sampling rates, the RMSE remains relatively insensitive to sampling rate for the first few values used in this study. For example, the RMSE in the eddy heat flux (Fig. 10c) increases from approximately 25W.m^2 at the most frequent sampling rate (1 day^{-1}), in the (turbulent) eastern sub-domain, corresponding to a relative error of ∼15% to 30W.m^2 (20% relative error) at the standard Argo sampling rate of 10.days^{-1}.

When comparing errors between the eastern and western sub-domains, it is clear from Fig. 10 that the error is greater over the eastern storm-track box than the western box. The error over the storm track box is ∼2 to ∼3 times higher than the equivalent error over the eastern region. The larger errors in turbulent region downstream underscore the results of section 4.1 that showed an underestimate of the high magnitude motions.

4.2.2. Effect of the Number of Floats

We now repeat the analysis of section 4.2.1, this time investigating the influence of the number of independent floats in the virtual array. The temporal sampling rate is held constant at the common Argo float sampling rate of 10 days. As in section 4.2.1, we compute the RMS errors between the model and reconstructed time mean meridional velocity, EKE and heat-flux, integrated over the two regions shown Fig. 9. The number of virtual floats is controlled by randomly sampling a fraction of the float trajectories from the complete data set. The fractions of the total number of floats selected are 1/16,1/8,2/8,3/8. . . 1.

The RMSE as a function of the total number of virtual floats for the each of the reconstructions are shown in Fig. 11. As should be expected, we find a decreasing RMSE for each of the fields considered with an increasing number of virtual floats. The RMSE, however, begins to approach a constant limit in both regions as the number of floats passes approximately 150. For example, as the number of floats increases from 28 (the smallest number used) to 112, the errors in the heat flux decrease from ∼120W.m^{-2} (a relative error of 50%)to 20Wm^{-2} (20% relative error) in the western (quiet) box and ∼180W.m^{-2} (65% relative error) to 40Wm^{-2} (30% relative error) in the western (storm track) box, a decrease of approximately 80% in both cases. However, increasing the number of floats fourfold from 112 to 450 results in RMSE reductions of between

5 and 10% in each region. As such there exists a certain number of floats which could be considered 'sufficient', given the diminishing returns in RMSE with an increasing number of floats.

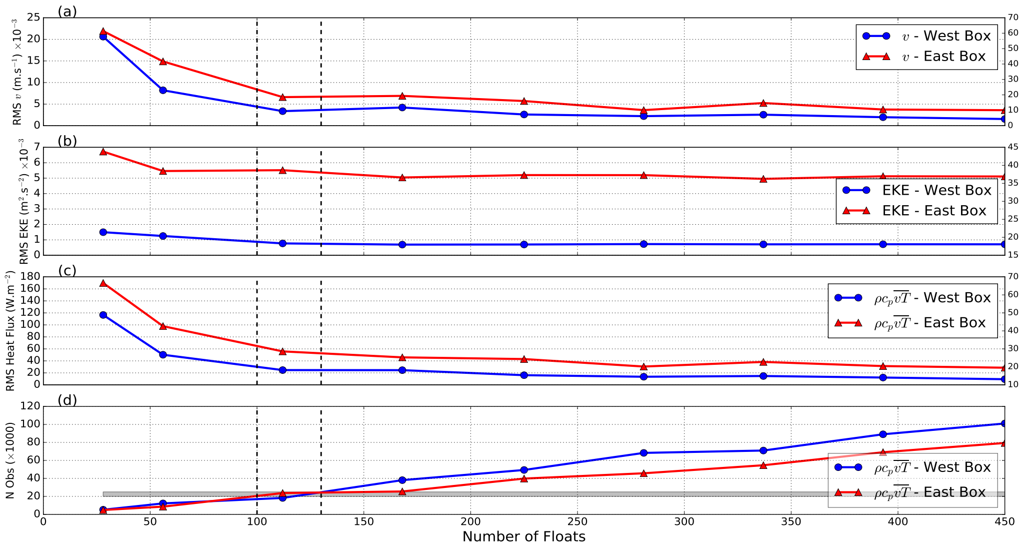

Figure 11: As in Fig. 10, but showing the change in the RMSE with variation in the number of virtual Lagrangian floats used in the reconstruction. Additional Panel (d) shows the total number of floats used in each reconstruction. Dashed black lines indicate the parameter regime occupied by Argo floats in the Southern Ocean, while the grey shaded region in panel (d) shows the equivalent number of observation density provided by Argo floats in the Southern Ocean

4.2.3. Effect of the Length of the Float Experiment

To conclude this section, we now investigate the effect of varying the length of float experiment from 1 to 10 years. The number of floats and temporal sampling rate are held constant at a value equivalent to the existing Argo array in the Southern Ocean (110 floats, which ensures that the number of floats per degree of longitude is similar to that of the current Argo array, with a sampling rate of 10 days). The RMSEs of the three chosen quantities are shown in Fig. 12. As with the number of floats, we find that the RMSE approaches a limit for all three quantities after the experiment has been running for 4 to 5 years, decreases from errors as high ranging from 90-100% in the eastern box in the case of the time-mean meridonal current and eddy heat flux after a single year float experiment, to 20-30% after 5 years. There is some suggestion of improvement in the meridional heat flux error (Fig. 12c) in the energetic eastern box throughout the 10 years of the experiment, with a reduction in the relative error from ∼20% to ∼10%. The decrease in the RMSE from 5 to 10 year is certainly not as significant as during the first 4 years of the simulation, where the RMSE decreased by 60-70%.

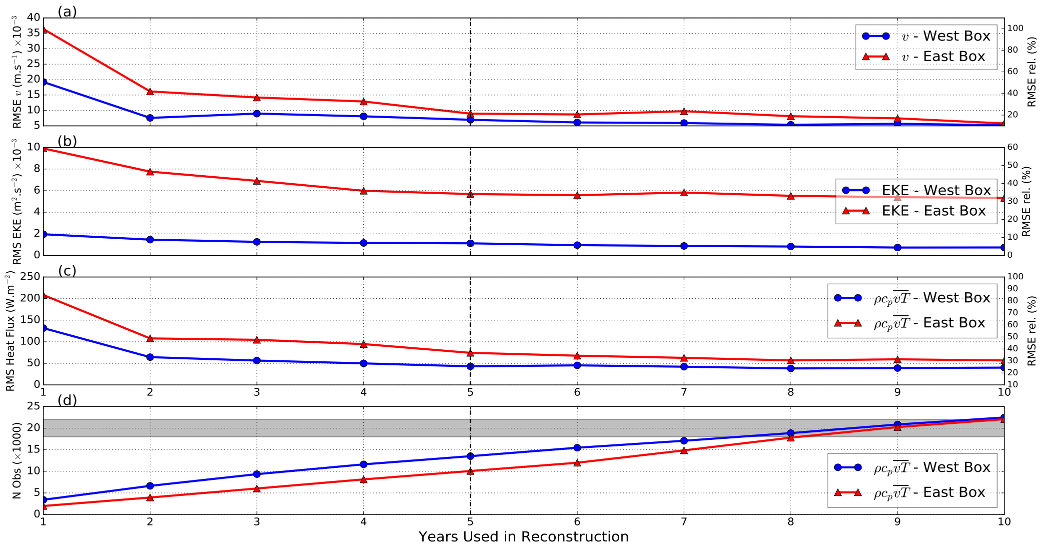

Figure 12: As in Fig. 10, but showing the change in the RMSE with variations in the number of years of Lagrangian data used in the reconstruction. Dashed black lines indicate the number of years in the ANDRO dataset Ocean, while the grey shaded region in panel (d) shows the equivalent number of observation density provided by Argo floats in the Southern Ocean

As with the previous discussion of the influence of the number of floats on the capacity on large scale reconstructions of oceanographic quantities, there appears to be diminishing returns in RMSE after approximately 4 years, with the first 5 years providing approximately 90% of the reduction in heat-flux RMSE and the final five years providing an additional 10% of error reduction.

5. Cross-frontal eddy-fluxes from Lagrangian drifters

Is it possible to use Lagrangian observations to estimate the cross-stream fluxes? This question is complicated by the fact that it is necessary to estimate not only the fluxes themselves, but also the front or streamline, which must be computed in a manner consistent with the computed fluxes. To understand the importance of consistent estimation of the streamlines, consider the time-mean flux density of some tracer, θ, written as $\mathbf{F}^\theta = \mathbf{u}\theta$. We can now form the time-mean "flux-streamline" from the time-mean flux by solving the differential equation:

$$\frac{d\overline{\mathbf{X}}}{ds} = \overline{\mathbf{F}}^\theta, \tag{11}$$

with initial condition $\mathbf{X}(0) = \mathbf{X}_0 = (x_0, y_0)$. In Eqn. 11, $\mathbf{X} = (X(s), Y(s))$ are respectively the zonal and meridional coordinates of the streamline, parameterized by the arc-length, s. By construction, there can be no time-mean transport across this streamline, as $\mathbf{F}^\theta \cdot \eta = 0$ everywhere along the curve, where η is the unit normal to $\mathbf{X}$. The streamline is not guaranteed to form a closed loop, even in a periodic domain, since integrating the y component of Eqn. 11 around the full circuit gives:

$$y_1 - y_0 = \oint \frac{dY}{ds} ds = \oint v\theta \; ds \tag{12}$$

where y_1 is the latitude of the streamline as it crosses its original longitude. $y_1 - y_0$ is not necessarily zero, as the flux $v\theta$ is not normal to the streamline and thus does not integrate to zero. Despite this fact, we note that in practice the difference between y_1 and y_0 is small. We take the latitude of the streamline as it crosses its original longitude x_0 to be y_1, such that $X(s_1) = (x_0, y_1)$, where s_1 is the total arc-length of the streamline as it completes a circumpolar circuit, and $y_1 \neq y_0$. If we close this curve by artificially extending it from

(x_0, y_1) to (x_0, y_0), then there can be a non-zero time mean flux across the curve, concentrated solely in the segment $(x_0, y_1) \rightarrow (x_0, y_0)$. Now, consider a new curve, $\mathbf{X'}$, with identical starting latitude and longitude as the streamline $\mathbf{X}$, that is $\mathbf{X'}(s_0) = (x_0, y_0)$, but constructed in such a way that it both forms a closed contour circling the domain, (i.e. it returns to (x_0, y_0)) and remains close to the original streamline $\mathbf{X}$. Since $\mathbf{X'} \cdot \eta \neq 0$ as the new curve is no longer aligned with the streamline defined by Eqn. 11, there will be small, but non-zero cross-stream flux distributed along the contour. Since the curves $\mathbf{X}$ and $\mathbf{X'}$ enclose similar areas, as long as $\mathbf{F}^\theta$ is smooth, then by Green's theorem, the total flux across each contour should also be similar. However, the *distribution* of this flux along each curve is likely to be very different, with any non-zero flux across $\mathbf{X}$ restricted to the $(x_0, y_1) \rightarrow (x_0, y_0)$ segment, while flux across $\mathbf{X'}$ is likely to be distributed along the contour. The origin of these fluxes could be due to the contour X' passing through a new region of enhanced eddy activity or, more likely, due to a misalignment of the streamline path and the mean flux. While the former phenomena is interesting and worthy of further study, the later simply indicates that the definition of the front does not follow the mean path of the circumpolar current.

As such, to unambiguously identify the source of a flux , we now decompose the time-mean tracer flux density into time-mean and perturbation components:

$$\overline{\mathbf{F}}^\theta = \overline{\mathbf{u}}\overline{\theta} + \overline{\mathbf{u}'\theta'}. \tag{13}$$

We can now compute a new streamline, $\overline{\mathbf{X}}$, defined as:

$$\frac{d\overline{\mathbf{X}}}{ds} = \overline{\mathbf{u}}\overline{\theta}, \tag{14}$$

with the initial conditions $\overline{X}(0) = (x_0, y_0)$. By construction, there can be no contribution to the total cross-stream flux from the mean component, as $\overline{\mathbf{u}}\overline{\theta} \cdot \eta = 0$ at all points on the curve. However, since $\overline{\mathbf{u}'\theta'} \cdot \eta \neq 0$, any significant fluxes must then arise solely from the eddy component. By using this special definition of a streamline, we are able to unambiguously identify the origins of the cross-frontal fluxes.

Local fluxes can be decomposed by the Helmholtz theorem into rotational and divergent components. The rotational fluxes necessarily non-divergent and they do not contribute to the to the local tracer balance. Thus, rotational fluxes have no direct dynamical effect on the flow field (Marshall and Shutts, 1981). However, rotational fluxes can dominate any local flux (Marshall and Shutts, 1981; Griesel et al., 2009). In this paper, we do not attempt to perform a Helmholtz decomposition to remove the rotational fluxes, as it is not obvious how this should be done using our Lagrangian observations. Furthermore, in a singly periodic domain, such as our model domain, no unique decomposition of the flux exists (Fox-Kemper et al., 2003). On the other hand, rotational fluxes, although they dominate term in local tracer budgets, tend to transport as much tracer into a region as they do out of it (Jayne and Marotzke, 2002). Thus summing over a region tends to cancel out the non-divergent fluxes (Griesel et al., 2009). As such, rather than attempting a Helmholtz decomposition, instead, we follow Griesel et al. (2009) and Dufour et al. (2015) and compute the cumulative sum of the across-front tracer transport. Doing so has the effect of removing the majority of the dynamically inert rotational fluxes, as the act of summing positive and negative rotational fluxes with similar magnitudes results in a large degree of self-cancellation.

5.1. Cross-frontal heat-fluxes in the numerical model

With the argument made in the previous subsection in mind, we now attempt to determine the cross-frontal eddy heat fluxes at 1000m depth in the numerical model. The cross-frontal heat flux density calculated in this section is defined:

$$F_\eta^\Theta(x,y) = c_p \rho \Theta(x,y) v_\eta(x,y) \Delta s \Delta z. \tag{15}$$

In Eqn. 14 c_p =4.0J.kg^{-1}.K^{-1} is the specific heat of sea-water at constant pressure, and ρ =1024kg.m^{-3} is the sea-water density.

For the purposes of comparison, two different frontal definitions are used. The first, which we call a ‘Lagrangian’ definition, is defined using the definition given in Eqn. 14, with initial conditions of $\mathbf{X}_0 = (0, L_y/2)$. The ‘mean’ flow in Eqn. 14 is taken from the reconstructed mean velocity field, $\overline{\mathbf{u}}$ obtained from the virtual Argo floats as described in section 4. Similarly, the mean conservative temperature field, Θ, is determined using the virtual Argo float temperature estimates (which are obtained by linearly interpolating the model fields to the float velocity measurement locations) using the same geographic binning methodology described in Sec. 3.4. The second definition, which we call 'Eulerian' is defined by direct integration of the hydrostatic equation from the surface to 1000m to obtain a geostrophic streamfunction, ψ_g, from which a streamfunction contour is selected as the front. For easy comparison between the Lagrangian and Eulerian fronts, we select the contour present at $\mathbf{X}_0 = (0, L_y/2)$. The Lagrangian and Eulerian fronts, together with the geostrophic streamfunction, are plotted in Fig. 13a. Although the definitions of each front differ, Fig. 13 shows very similar trajectories. Differences in the location of the fronts generally occur only at small scales. We also note that the Eulerian front, by definition, returns to its initial location after a full circuit of the domain. In contrast, the Lagrangian front does not exactly return to its starting location. However, the difference between the front's initial and final location is less than 20km.

The cross-frontal eddy heat flux is now estimated by the virtual Argo floats in a manner almost identical to the method used to reconstruct the gridded fields in Section 4: all float observations within 100km of a point on the front are collected, resolved into along and across front components and the ensemble is averaged. We compute the eddy heat flux from the virtual Argo floats across both the Eulerian and Lagrangian contour, which allows us to evaluate the influence of the choice of contour definition on the resulting reconstruction. We also compute the eddy heat-flux across the Eulerian front directly from the model output. This value is taken as the 'true' value for the purposes of computing error statistics.

The structure of the cross-frontal heat flux is shown in Fig 13b for each of our estimates. The directly computed heat flux (the 'true' value, red curve in Fig. 13b) shows a very similar structure to that discussed by Abernathey and

Cessi (2014): there is an increased *southward* heat flux in the storm-track region directly downstream of the topographic feature in the largest standing meander. This localized southward heat-flux is somewhat moderated by a northward heat-flux further upstream, consistent with the mechanism proposed by Abernathey and Cessi (2014) (see their Fig. 3).

When estimating the cross-frontal heat-flux using the virtual Argo floats, we report mixed results. While the estimates made using the virtual floats capture the enhanced southward eddy heat-flux downstream of the topography, only the flux estimated across the Eulerian contour captures the northward heat flux further downstream. Investigating the source of this error reveals that the Lagrangian contour does not produce a large enough secondary standing meander and, as such, the northward heat flux is not represented.

The RMS error at each point on the contour is shown for the virtual Argo float derived heat flux estimates in Figure 13c, where it is easily seen that for both contours the error peaks in the storm-track region downstream of the topography. Although the mean heat-flux error in this region is a factor of four larger than in the less energetic upstream region (defined over the boxes described in Section 4) the error relative to the heat-flux magnitude, $\epsilon_r = (F^{\text{estimated}} - F^{\text{exact}})/F^{\text{exact}}$ remains roughly constant over the domain (not shown). The fact that the heat-flux error scales with the magnitude of the underlying heat flux is consistent with the discussion in Section 4, where it was shown that both mean and eddy errors were significantly higher in the storm-track region when compared with those in the quiet upstream region.

The cumulative fluxes, plotted in Fig. 13d, assuming a layer thickness of 100m, show that the basic qualitative spatial structure of the cross-frontal heat flux captured by the Lagrangian observations, with the net southward heat flux concentrated in the energetic region downstream of the topography, and little significant heat flux outside of this region. Quantitatively, the southward heat flux is underestimated by the Lagrangian observations. The heat-flux is approximately 2 to 2.5 times smaller in the storm-track region when compared to the heat flux estimated directly from the model output. It is also notable that

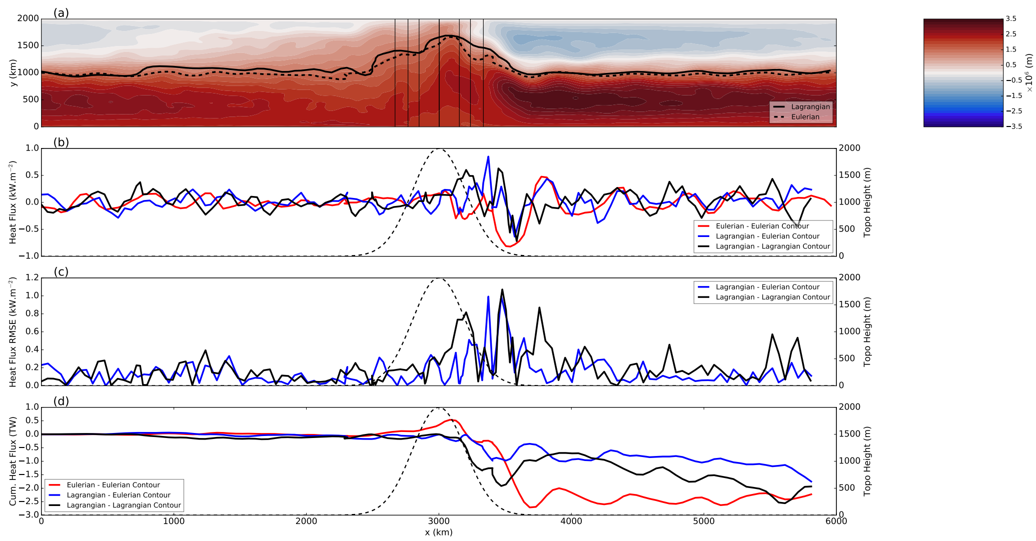

Figure 13: The cross stream heat flux at 1000m calculated directly from the numerical model and estimated from the virtual Argo floats. (a) The model time-mean geostrophic stream-function ψ_g. The solid black line (labelled “Lagrangian”) indicates the streamline used for the heat-flux calculation determined from the virtual Argo floats, while the dashed line (labelled “Eulerian”) is the equivalent streamline computed directly from the numerical model fields; (b) cross-stream heat flux computed directly from the numerical model across the “Eulerian” contour (red); from the virtual Argo floats across the “Eulerian” contour (blue); and from the virtual Argo floats across the “Lagrangian” contour (blue); (c) the root mean squared error (RMSE) for the heat flux estimated by the virtual Argo floats across the Eulerian (blue) and Lagrangian (black) contour; and (d) the cumulative heat flux along the contours.

there is a slow drift in the heat flux estimated across the Lagrangian contour. We have not been able to identify the source of this drift, but as the Lagrangian contour and the Eulerian contour are not perfectly aligned, small fluxes across this contour can easily accumulate into a significant net southward heat flux.

The results of this section indicate that the uncertainty in the cross-frontal heat flux is as sensitive to the exact definition of the contour itself as it is to the underlying errors from the use of finite number of Lagrangian observations in its reconstruction. Small changes in a contour's location or orientation appear to result in large localized differences in the flux across the contour. However, despite these problems, the cross-frontal heat flux from the virtual Argo floats captures the broad scale quantitative heat flux structure, correctly determining the localisation of the heat-flux downstream of the bathymetry, as well as providing a quantitative estimate that correctly captures the heat-flux's order of magnitude. These results provide some confidence that the existing Argo array can be used to study heat-fluxes in the real ocean.

6. Reconstruction of Deep Mean and Eddy Fluxes in the Southern Ocean from Argo Floats

We now employ the lessons learned from the numerical simulation to the problem of estimating the mean and cross-frontal heat flux in the Southern Ocean using the Argo array of floats between 2005 and 2011. Here, we make use of the ANDRO dataset and the associated Argo hydrographic profiles, described in Section 3. Additionally, we model the error in the velocity estimates as a sum of instrumental error, $\epsilon_{\mathbf{u}_{\text{inst.}}}$ which includes the error due to shear in the water column and is included with the ANDRO dataset, and the sampling error, $\epsilon_{\mathbf{u}_{\text{samp.}}}$. The sampling error is simulated by direct Monte-Carlo methods. For each velocity estimate, 1000 simulated velocity errors are drawn from a normal distribution with mean and standard deviations determined from orthogonal regression of the virtual Argo float errors described in Section 4.1 (see Fig. 7) from the float experiment with parameters most appropriate to the Southern

Ocean Argo array (that is, 5 years experiment duration, 10 day sampling period and 110 floats). Thus the error dependence on velocity is included in the error model. The final error values are the instrumental and sampling errors summed in quadrature.

6.1. Time Mean Circulation and Heat Flux

The time-mean speed and heat flux at 1000m depth are estimated using the procedure described in Section 3 and displayed in Fig. 14. The mean speed maps (Fig. 14a) are essentially identical to those produced by Ollitrault and Colin de Verdiére (2014) (see their Fig. 10) using the same dataset and show numerous features, such as quasi-zonal jets associated with the Antarctic Circumpolar Current (ACC), topographic steering of those jets, strong boundary currents and stationary meanders that are all known phenomena in the Southern Ocean (Rintoul and Garabato, 2013). Current speeds of up to 25cm/s are found in the boundary currents and in the ACC jet cores. The meridional heat flux (Fig. 14b) shows enhanced values along the core of the ACC and downstream of large bathymetric features where the heat flux is organized into a alternating northward/southward bands due to the presence of standing meanders, reminiscent of the high resolution numerical simulations of Griesel et al. (2009) (see, for example, their Fig. 3). The fact that these mean fields produce a large number of the expected features of the Southern Ocean's circulation indicate that there are sufficient observations within the ANDRO dataset, with sufficient geographic coverage, that it is capable of producing at least qualitatively accurate mean fields.

The error field, shown in Fig. 14c. Errors are limited to less than 30 cm.s^{-1} throughout the Southern Ocean, and are found to be higher in regions associated with strong jets or downstream of topographic features. However, the contrast between regions is not large and and the estimated errors generally vary less than 10 cm.s^{-1} across the basin, consistent with the results of the idealized numerical model.

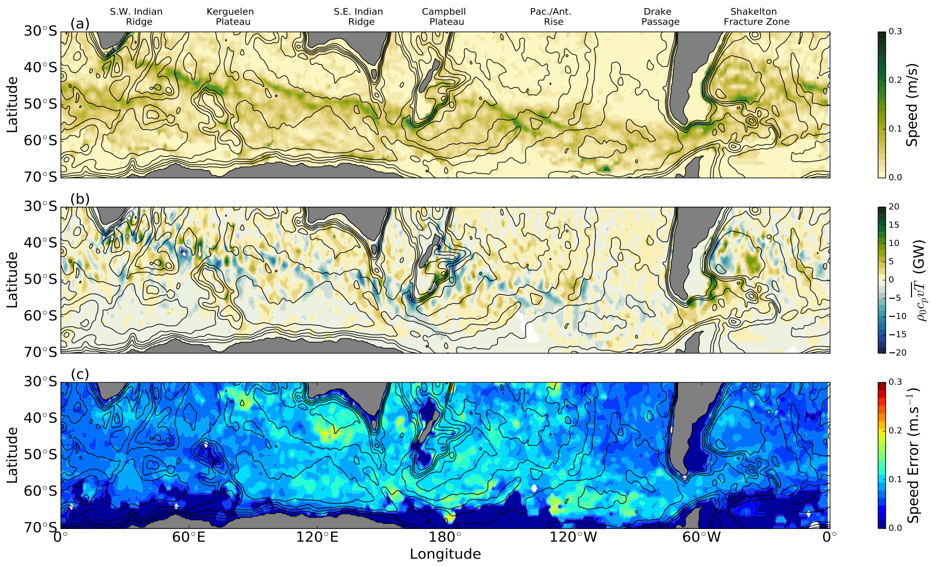

Figure 14: Time mean (a) speed; (b) meridional heat flux ($\rho_0 c_p \overline{vT}$) in the 950-1150db layer, reconstructed from the ANDRO float derived current velocities and Argo temperature profiles; and (c) estimated speed error including both instrumental and sampling errors. Thin black contours are the bathymetry (CI:1000m)

6.2. Cross-Frontal Eddy Heat Flux

We now compute the heat flux across a circumpolar contour that approximates a mean streamline at this depth. To determine this streamline, we follow the procedure outlined in Section 5: we integrate Eqn. 14 numerically (as before with a 4th order Runge-Kutta scheme), using the time-mean velocity and conservative temperature fields and assume a layer thickness of 150m. The latitude of the contour at 0° longitude is set to 48°S, corresponding to the approximate location of the polar front determined by Dufour et al. (2015) in a high resolution model. The location of this contour and bathymetry taken from the ETOPO01 dataset (Amante and Eakins, 2009) is plotted in Fig. 15a. This contour follows a similar pathway to previous calculations of the polar front (e.g. Dufour et al. (2015)) and, as such, we take this contour to be the polar front (although it should be noted that circumpolar 'contour' definitions of fronts have several limitations, e.g. Chapman (2014, 2017)). We note as well that although the observational sampling density along this streamline is approximately constant, there is a reduction of approximately 50% in the south west Pacific region, between approximately 100°W and 80°W. As such, the sampling error estimates in this region are likely optimistic. We have repeated this calculation with more pessimistic parameter settings and obtained similar overall error estimates, indicating that the dominant source of uncertainty in the oceanic system is likely internal variability.

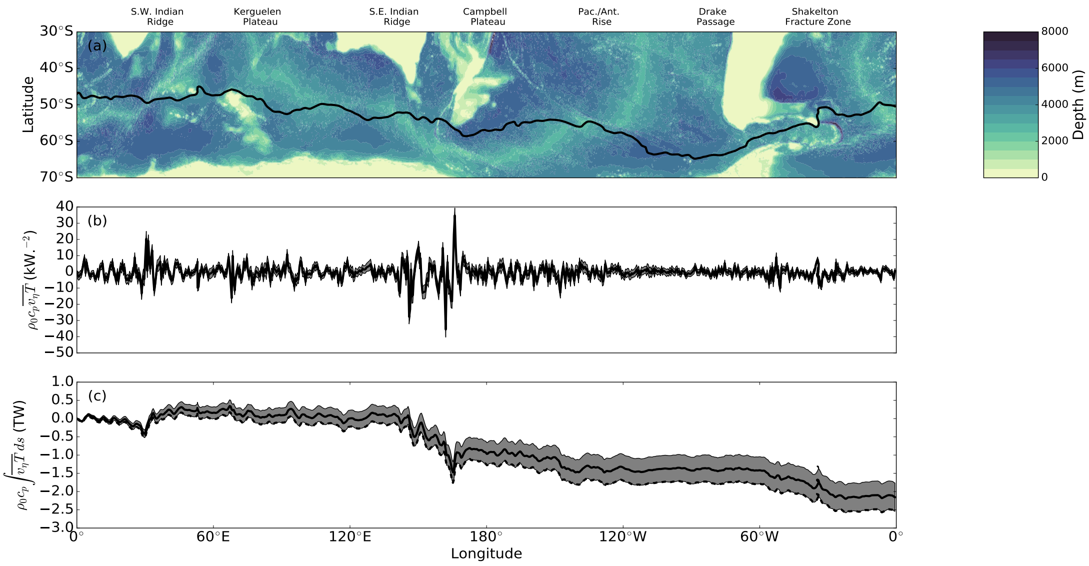

Figure 15: Heat-flux across the polar front estimated from the ANDRO dataset and the Argo temperature profiles. (a) the time-mean position of the polar front overlaying the bathymetry from the ETOPO01 dataset; (b) the cross frontal heat-flux ($\rho c_p \overline{vT} \Delta s \Delta z$); (c) the cumulative cross-frontal heat-flux. Shaded grey regions in panels (a) and (b) indicate the 3σ error bounds

The local eddy heat flux across the polar front is shown in Fig. 15b. As in Thompson and Sallée (2012) and Dufour et al. (2015), we find that the eddy heat flux is localized in 'hot-spot' regions where either the front crosses large bathymetric features (labeled in Fig. 15a) such as the Campbell Plateau and through Drake Passage, or in adjacent downstream regions. The magnitude of the eddy heat flux averaged over regions where bathymetry is shallower than 1500 is approximately 2.5 greater than in deeper regions. Although the magnitude of the cross-frontal heat flux increases in the regions with important bathymetry, it is important to note that the eddy heat flux shows large positive and negative fluctuations that cancel upon integration along the frontal contour.

Integrating along the polar front removes the rotational component of the eddy flux and gives the cumulative transport (Fig. 15c), which further underscores the importance of hot-spots in the Southern Ocean heat-transport. Unlike the local heat flux, the cumulative fluxes are organized into a series of generally southward step-changes (although a small northward heat flux is found in the vicinity of the Southwest Indian Ridge at approximately 30°E). Large southward heat transports are found near the Southeast Indian Ridge south of Tasmania (longitude: $\sim$145°E, heat transport: $\sim$0.75TW) the Campbell Plateau ($\sim$170°E, $\sim$1.0TW), the Pacific Antarctic Rise ($\sim$130°W, $\sim$0.25TW) and through Drake Passage and the nearby Shackleton Fracture Zone/Scotia Arc ($\sim$50°W, $\sim$0.75TW). In total, the ANDRO dataset reveals approximately 2$\pm$0.5TW of heat transport across the polar front at 1000m depth. More than 90% of the total heat transport is occurs in less than 20% of the total longitudes spanned by the contour.

As Dufour et al. (2015) found in their high resolution numerical model, the ANDRO data reveal that the eddy heat flux is strongly concentrated in 'hot-spot' regions near large bathymetric features. The concordance between our results and those of Dufour et al. (2015) is remarkable, given the supposed sparseness of the Argo float observations in the ocean. However, the results of the modelling component of this study give us confidence that the results presented in this section are valid, although subject to error. Improvement of the mapping procedure, as well as the inclusion of additional deep drifter datasets, such as RAFOS floats, could further increase confidence in the results presented here.

7. Discussion and Conclusions

In this paper we have used 'virtual' Argo floats advected in an idealized model of the Southern Ocean to critically assess the ability of the existing Argo array to reconstruct both the time-mean and eddying quantities of importance to the general circulation. Comparing time-mean and eddy quantities reconstructed from the virtual Argo floats directly to the model fields reveals that, at float observation densities similar to those available from the Argo array, it is possible to robustly reconstruct several important quantities, including quadratic perturbation quantities such as the EKE and eddy heat flux. We have tested, systematically, the influence of temporal sampling frequency, the number of floats and the time span of the float experiment, and found, in all case, that robust reconstructions of the these quantities is possible, even when relatively 'pessimistic' values of these parameters are chosen. We have also shown that is is also possible to reconstruct cross-frontal eddy heat fluxes using only the Lagrangian floats, but only for specially defined frontal contours that may not necessarily form closed circumpolar contours. As such, this study echoes previous work (Davis, 1987, 1991b) who showed that comparatively few surface drifters were required to resolve an idealized thin western boundary current.

The key result of this study is that, with a sufficient number of floats tracked over a sufficiently long period of time, one can reconstruct with a high degree of fidelity both time-mean fields and the local eddy statistics. The challenge is, of course, to define how long a 'sufficiently' long time period is, and how many floats are 'sufficient'. There are no clear answers to these questions, as any response would depend on the needs of the particular study. However, the results of the numerical modeling portion of this study indicate that the current observational coverage and sampling rates provided by Argo floats in the Southern Ocean return reconstruction errors that are not substantially improved by the addition of more floats or longer float experiments (although extending the life of the Argo project is essential for long term climate monitoring), and only marginally improved by increasing the sampling rate. The reasons for the observed asymptotic error performance are not clear. However, a similar OSSE performed by Kamenkovich et al. (2011) noted that reconstruction errors were generally smaller in regions with higher absolute current speeds, where the oceanic ‘signal’ is able to dominant the ‘noise’ introduced by the reconstruction error. In the Southern Ocean, where currents are consistently strong, the signal to noise ratio could well be large enough that the oceanic signal can be defined with relatively few samples. In our model study, there are relatively small differences in the reconstruction error of the time mean meridional velocity between the eastern (where time mean currents are weaker) and western (where time mean currents are stronger) sub-domains, despite the enhanced variability in the later region, which provides some limited evidence that the effect described by Kamenkovich et al. (2011) may explain the relative insensitive of the reconstruction error to the number of samples - provided a minimum number of samples has been obtained.

Although we have shown that increasing the float profiling rate (and hence sampling rate) results a reduction in the error of the resulting estimates of the both mean and eddying quantities, doing so would, in reality, reduce the lifetimes of the floats which are generally inversely proportional to the number of cycles (Roemmich et al., 2009). Although increasing the sampling rate would not necessarily reduce the total number of profiles collected by a particular float, it would reduce the length of the float experiment and, potentially, restrict the geographical range sampled by the float.

With the results obtained from the numerical model in mind, we have then used the existing array of Argo float to compute the eddy heat-flux across the Polar Front in the Southern Ocean, building upon similar work using the smaller ALACE float array (Gille, 2003a,b). The numerical model allows us to construct a suitable model for the errors induced by the discrete temporal sampling for inclusion alongside errors due to vertical shear in the water column and uncertainty due to internal variability within the ocean which are obtained either from the ANDRO dataset or estimated directly. We find that these errors, although important, do not impede the calculation of the cross-frontal eddy heat-flux at this depth. Our results are qualitatively very similar to those obtained by Griesel et al. (2009) and Dufour et al. (2015) in a high resolution numerical model, which, together with the results from our own modeling study, allow us to place a fairly high degree of confidence in the capacity of Argo floats to reconstruct the heat flux and other eddy quantities.

Our study does, however, contain some notable shortcomings. For example, the idealized model configuration was used primarily for convenience and although it produces a flow field reminiscent of the that in the Southern Ocean, the actual ocean circulation is, in reality, far more complex and contains numerous phenomena unrepresented in our model. Additionally, as shown by Rosso et al. (2014) in a series of progressively higher resolution numerical models, 5km grid spacing is not sufficient to completely resolve the oceanic mesoscale, and certainly not the energetic sub-mesoscale. As such, the length scales of important features in the Southern Ocean are likely smaller than can be resolved by our simulation, and it is still an open question if discretely sampled Argo floats would be able to accurately represent the eddy fluxes under these conditions. A similar analysis to the present work, conducted using the output of a high-resolution realistic model configuration, could be illuminating.

With the shortcomings of this study noted, we finish on a note of optimism: the evidence presented here suggests that the current Argo array is able to generate reliable eddy statistics and that the addition of additional floats to the system are not strictly necessary for this puropose, as they are not likely to dramatically improve the capacity of the array to represent meso-scale statistics, although additional floats are likely to aid resolving important features in undersampled regions. Thus, a promising avenue of future research is to exploit the Argo array to close local tracer budgets. In particular, the flux of biogeochemical tracers across fronts, a quantity of great importance to the climate system, could be estimated using the developing array of 'bio-Argo' floats, capable of measuring biogeochemical quantities such as carbon and nutrients. Additionally, with the continuing improvement and maintenance of the Argo array, long term monitoring of eddying quantities over broad regions may also be possible.

Acknowledgement

C.C. was funded by a National Science Foundation Division of Ocean Sciences Postdoctoral Fellowship 1521508. J.B.S. received support from Agence Nationale de la Recherche (ANR), grant number ANR-12-PDOC-0001. Numerical calculations were were undertaken on the OCCIGEN supercomputer managed by the French *Centre Informatique National de l'Enseignement Supérieur*. Supercomputing resources were allocated by the *Grand Équipement National de Calcul Intensif* under the SO-BRIGHT project. The authors acknowledge two anonymous reviewers whose comments greatly improved the manuscript, as well as a third anonymous reviewer on a previous version of this paper who explained the importance of consistent flux streamline estimation.

References

Abernathey, R., Cessi, P., 2014. Topographic enhancement of eddy efficiency in baroclinic equilibration. Journal of Physical Oceanography 44, 2107–2126.

Abernathey, R., Marshall, J., Ferreira, D., 2011. The dependence of southern ocean meridional overturning on wind stress. Journal of Physical Oceanography 41, 2261–2278. doi:10.1175/JPO-D-11-023.1.

Amante, C., Eakins, B., 2009. ETOPO1 1 Arc-Minute Global Relief Model: Procedures, Data Sources and Analysis. NOAA Technical Memorandum NESDIS NGDC-24.. National Geophysical Data Center, NOAA. doi:10.7289/V5C8276M.

Arbic, B.K., Mller, M., Richman, J.G., Shriver, J.F., Morten, A.J., Scott, R.B., Srazin, G., Penduff, T., 2014. Geostrophic turbulence in the frequencywavenumber domain: Eddy-driven low-frequency variability. Journal of Physical Oceanography 44, 2050–2069. doi:10.1175/JPO-D-13-054.1.

Arbic, B.K., Scott, R.B., Flierl, G.R., Morten, A.J., Richman, J.G., Shriver, J.F., 2012. Nonlinear cascades of surface oceanic geostrophic kinetic energy in the frequency domain. Journal of Physical Oceanography 42, 1577–1600. doi:10.1175/JPO-D-11-0151.1.

Barnier, B., Siefridt, L., Marchesiello, P., 1995. Thermal forcing for a global ocean circulation model using a three-year climatology of ecmwf analyses. Journal of Marine Systems 6, 363–380.

Chapman, C.C., 2014. Southern ocean jets and how to find them: Improving and comparing common jet detection methods. Journal of Geophysical Research: Oceans 119, 4318–4339. doi:10.1002/2014JC009810.

Chapman, C.C., 2017. New perspectives on frontal variability in the southern ocean. Journal of Physical Oceanography 47, 1151–1168. doi:10.1175/JPO-D-16-0222.1.

Chapman, C.C., Hogg, A.M., Kiss, A.E., Rintoul, S.R., 2015. The dynamics of southern ocean storm tracks. Journal of Physical Oceanography 45, 884–903.

Davis, R., 1982. On relating eulerian and lagrangian velocity statistics: Single particles in homogeneous flows. Journal of Fluid Mechanics 114, 1–26. doi:10.1017/S0022112082000019.

Davis, R.E., 1987. Modeling eddy transport of passive tracers. Journal of Marine Research 45, 635–666.

Davis, R.E., 1991a. Lagrangian ocean studies. Annual Review of Fluid Mechanics 23, 43–64. doi:10.1146/annurev.fl.23.010191.000355.

Davis, R.E., 1991b. Observing the general circulation with floats. Deep Sea Research Part A. Oceanographic Research Papers 38, S531 – S571. doi:10.1016/S0198-0149(12)80023-9.

Davis, R.E., 1998. Preliminary results from directly measuring middepth circulation in the tropical and south pacific. Journal of Geophysical Research: Oceans 103, 24619–24639. doi:10.1029/98JC01913.

Dufour, C.O., Griffies, S.M., de Souza, G.F., Frenger, I., Morrison, A.K., Palter, J.B., Sarmiento, J.L., Galbraith, E.D., Dunne, J.P., Anderson, W.G., et al., 2015. Role of mesoscale eddies in cross-frontal transport of heat and biogeochemical tracers in the southern ocean. Journal of Physical Oceanography 45, 3057–3081.

Elipot, S., Lumpkin, R., Perez, R.C., Lilly, J.M., Early, J.J., Sykulski, A.M., 2016. A global surface drifter data set at hourly resolution. Journal of Geophysical Research: Oceans 121, 2937–2966. doi:10.1002/2016JC011716.

Fox-Kemper, B., Ferrari, R., Pedlosky, J., 2003. On the indeterminacy of rotational and divergent eddy fluxes. Journal of Physical Oceanography 33, 478–483. doi:10.1175/1520-0485(2003)033<0478:OTIORA>2.0.CO;2.

Fratantoni, D.M., Richardson, P.L., 1999. Sofar float observations of an intermediate-depth eastern boundary current and mesoscale variability in the eastern tropical atlantic ocean. Journal of Physical Oceanography 29, 1265–1278. doi:10.1175/1520-0485(1999)029<1265:SFOOAI>2.0.CO;2.

Gille, S.T., 2003a. Float observations of the southern ocean. part i: Estimating mean fields, bottom velocities, and topographic steering. Journal of Physical Oceanography 33, 1167–1181.

Gille, S.T., 2003b. Float observations of the southern ocean. part ii: Eddy fluxes. Journal of Physical Oceanography 33, 1182–1196.

Griesel, A., Gille, S.T., Sprintall, J., McClean, J.L., Maltrud, M.E., 2009. Assessing eddy heat flux and its parameterization: A wavenumber perspective from a 1/10 ocean simulation. Ocean Modelling 29, 248 – 260. doi:http://dx.doi.org/10.1016/j.ocemod.2009.05.004.

Hoffman, R.N., Atlas, R., 2016. Future observing system simulation experiments. Bulletin of the American Meteorological Society 97, 1601–1616. doi:10.1175/BAMS-D-15-00200.1.

Jayne, S.R., Marotzke, J., 2002. The oceanic eddy heat transport. Journal of Physical Oceanography 32, 3328–3345. doi:10.1175/1520-0485(2002)032<3328:TOEHT>2.0.CO;2.

Kamenkovich, I., Cheng, W., Sarachik, E.S., Harrison, D.E., 2009. Simulation of the argo observing system in an ocean general circulation model. Journal of Geophysical Research: Oceans 114. doi:10.1029/2008JC005184. c09021.

Kamenkovich, I., Cheng, W., Schmid, C., Harrison, D.E., 2011. Effects of eddies on an ocean observing system with profiling floats: Idealized simulations of the argo array. Journal of Geophysical Research: Oceans 116, n/a–n/a. URL: http://dx.doi.org/10.1029/2010JC006910, doi:10.1029/2010JC006910. c06003.

Keating, S.R., Smith, K.S., Kramer, P.R., 2011. Diagnosing lateral mixing in the upper ocean with virtual tracers: Spatial and temporal resolution dependence. Journal of Physical Oceanography 41, 1512–1534. doi:10.1175/2011JPO4580.1.

LaCasce, J., 2008. Statistics from lagrangian observations. Progress in Oceanography 77, 1–29. doi:10.1016/j.pocean.2008.02.002.

Lebedev, K.V., Yoshinari, H., Maximenko, N.A., Hacker, P.W., 2007. YoMaHa'07: Velocity data assessed from trajectories of argo floats at parking level and at the sea surface. IPRC Technical Note 4.

Maas, L.R.M., 1989. A comparison of eulerian and lagrangian current measurements. Deutsche Hydrografische Zeitschrift 42, 111–132. doi:10.1007/BF02226290.

Madec, G., 2014. Nemo ocean engine. Note du Pôle de modélisation, Institut Pierre-Simon Laplace (IPSL) 27.

Majkut, J.D., Carter, B.R., Frölicher, T.L., Dufour, C.O., Rodgers, K.B., Sarmiento, J.L., 2014. An observing system simulation for southern ocean carbon dioxide uptake. Philosophical Transactions of the Royal Society of London A: Mathematical, Physical and Engineering Sciences 372. doi:10.1098/rsta.2013.0046.

Marshall, J., Shutts, G., 1981. A note on rotational and divergent eddy fluxes. Journal of Physical Oceanography 11, 1677–1680. doi:10.1175/1520-0485(1981)011<1677:ANORAD>2.0.CO;2.

McDougall, T.J., Barker, P.M., 2011. Getting started with TEOS-10 and the Gibbs Seawater (GSW) oceanographic toolbox. SCOR/IAPSO WG 127, 1–28.

Middleton, J.F., 1985. Drifter spectra and diffusivities. Journal of Marine Research 43, 37–55. doi:doi:10.1357/002224085788437334.

Ollitrault, M., Rannou, J.P., 2013. Andro: An argo-based deep displacement dataset. Journal of Atmospheric and Oceanic Technology 30, 759–788.

Ollitrault, M., Colin de Verdiére, A., 2014. The ocean general circulation near 1000-m depth. Journal of Physical Oceanography 44, 384–409.

Richardson, P.L., Fratantoni, D.M., 1999. Float trajectories in the deep western boundary current and deep equatorial jets of the tropical atlantic. Deep Sea Research Part II: Topical Studies in Oceanography 46, 305 – 333. doi:http://dx.doi.org/10.1016/S0967-0645(98)00100-3.

Ridgway, K., Dunn, J., Wilkin, J., 2002. Ocean interpolation by four-dimensional weighted least squares-application to the waters around australasia. Journal of atmospheric and oceanic technology 19, 1357–1375.

Rintoul, S.R., Garabato, A.C.N., 2013. Chapter 18 - dynamics of the southern ocean circulation, in: Gerold Siedler, Stephen M. Griffies, J.G., Church, J.A. (Eds.), Ocean Circulation and Climate A 21st Century Perspective. Academic Press. volume 103 of *International Geophysics*, pp. 471 – 492. doi:10.1016/B978-0-12-391851-2.00018-0.

Riser, S.C., Freeland, H.J., Roemmich, D., Wijffels, S., Troisi, A., Belbéoch, M., Gilbert, D., Xu, J., Pouliquen, S., Thresher, A., et al., 2016. Fifteen years of ocean observations with the global argo array. Nature Climate Change 6, 145–153.

Roach, C.J., Balwada, D., Speer, K., 2016. Horizontal mixing in the southern ocean from argo float trajectories. Journal of Geophysical Research: Oceans 121, 5570–5586. doi:10.1002/2015JC011440.

Roemmich, D., Johnson, G.C., Riser, S., Davis, R., Gilson, J., Owens, W.B., Garzoli, S.L., Schmid, C., Ignaszewski, M., 2009. The argo program: Observing the global ocean with profiling floats. Oceanography 22. doi:10.5670/oceanog.2009.36.

Rosso, I., Hogg, A.M., Strutton, P.G., Kiss, A.E., Matear, R., Klocker, A., van Sebille, E., 2014. Vertical transport in the ocean due to sub-mesoscale structures: Impacts in the kerguelen region. Ocean Modelling 80, 10 – 23. doi:10.1016/j.ocemod.2014.05.001.

Rupolo, V., 2007. A lagrangian-based approach for determining trajectories taxonomy and turbulence regimes. Journal of Physical Oceanography 37, 1584–1609. doi:10.1175/JPO3038.1.

Rupolo, V., Artale, V., Hua, B.L., Provenzale, A., 1996. Lagrangian velocity spectra at 700 m in the western north atlantic. Journal of Physical Oceanography 26, 1591–1607. doi:10.1175/1520-0485(1996)026<1591:LVSAMI>2.0.CO;2.

van Sebille, E., Johns, W.E., Beal, L.M., 2012. Does the vorticity flux from agulhas rings control the zonal pathway of nadw across the south atlantic? Journal of Geophysical Research: Oceans 117. doi:10.1029/2011JC007684. c05037.

van Sebille, E., Kamenkovich, I., Willis, J.K., 2011. Quasi-zonal jets in 3-d argo data of the northeast atlantic. Geophysical Research Letters 38. doi:10.1029/2010GL046267. l02606.

Smith, S., 1997. The Scientist and Engineer's Guide to Digital Signal Processing. California Technical Pub. URL: https://books.google.fr/books?id=rp2VQgAACAAJ.

Taylor, G.I., 1938. The spectrum of turbulence. Proceedings of the Royal Society of London A: Mathematical, Physical and Engineering Sciences 164, 476–490. doi:10.1098/rspa.1938.0032.

Thompson, A.F., Sallée, J.B., 2012. Jets and topography: Jet transitions and the impact on transport in the antarctic circumpolar current. Journal of physical Oceanography 42, 956–972.

Williams, R.G., Wilson, C., Hughes, C.W., 2007. Ocean and atmosphere storm tracks: The role of eddy vorticity forcing. Journal of Physical Oceanography 37, 2267–2289.

Willis, J.K., Fu, L.L., 2008. Combining altimeter and subsurface float data to estimate the time-averaged circulation in the upper ocean. Journal of Geophysical Research: Oceans 113. doi:10.1029/2007JC004690. c12017.

Wunch, C., 2006. Discrete Inverse and State Estimation Problems. Cambridge University Press, New York. URL: www.cambridge.org/9780521854245.